JOURNAL OF SPACECRAFT AND ROCKETS
Vol. 51, No. 3, May–June 2014

Supersonic Retropropulsion Computational Fluid Dynamics Validation with Langley 4 × 4 Foot Test Data

Daniel Guy Schauerhamer*
NASA Johnson Space Center, Houston, Texas 77058
Kerry A. Zarchi†
NASA Ames Research Center, Moffett Field, California 94035
and
William L. Kleb,‡ Jan-Reneé Carlson,§ and Karl. T. Edquist¶
NASA Langley Research Center, Hampton, Virginia 23681

DOI: 10.2514/1.A32693

Validation of computational fluid dynamics for supersonic retropropulsion is shown through the comparison of three Navier–Stokes solvers and wind-tunnel test results. The test was designed specifically for computational fluid dynamics validation and was conducted in the NASA Langley Research Center supersonic 4 × 4 foot Unitary Plan Wind Tunnel. The test includes variations in the number of nozzles, Mach and Reynolds numbers, thrust coefficient, and angles of orientation. Code-to-code and code-to-test comparisons are encouraging, and possible error sources are discussed.

Nomenclature

A_{ref}	=	19.63 in.^{2}, reference area
$C_{A,\text{aero}}$	=	aerodynamic contribution to axial force coefficient
$C_{A,\text{total}}$	=	$C_T + C_{A,\text{aero}}$, total axial force coefficient
C_m	=	pitching moment coefficient
C_N	=	normal force coefficient
C_P	=	pressure coefficient
C_T	=	T/qA_{ref}, thrust coefficient
L	=	10.2 in., model length
L_{ref}	=	5.0 in., reference length
$P_{o,\text{jet}}$	=	jet total pressure, psia
q	=	dynamic pressure, psia
R	=	2.5 in., model radius
Re	=	Reynolds number
r	=	radial coordinate, in.
T	=	thrust, lbf
$T_{o,\text{jet}}$	=	jet total temperature, °R
X	=	axial coordinate, in.
α	=	angle of attack, deg
σ	=	standard deviation calculated from wind-tunnel residuals
ϕ	=	roll angle, deg

I. Introduction

SUPERSONIC retropropulsion (SRP) is a viable means for deceleration of high-mass vehicles entering into the Martian atmosphere. Previous methods of deceleration are not scalable for exploration-type vehicles, which can potentially weigh tens of metric tons [1–6]. Because ground and flight testing of SRP at entry conditions can be difficult and cost-prohibitive, the development of this enabling technology can be enhanced with the ability to predict the flowfield numerically using computational fluid dynamics (CFD).

SRP results in a complex flow structure involving shocks, shear layers, recirculation, and stagnation regions. Correctly predicting these flow features will influence the accuracy of surface pressure distributions, forces and moments, and flow unsteadiness and makes validation of the CFD methods a high priority. The validation process includes using multiple CFD codes to compare to historical [7] and recent wind-tunnel tests [8]. Through code-to-code and code-to-test comparisons, best practices in gridding, numerical method selection, and solution advancement are established, and validity is added to the CFD methods for these flow physics. With that validity, confidence is built for using CFD to predict those same physics in Mars entry conditions.

Three CFD codes are being applied to SRP: Data Parallel Line Relaxation (DPLR) [9], Fully Unstructured Navier–Stokes Three-Dimensional (FUN3D) [10,11], and OVERset grid FLOW solver (OVERFLOW) [12]. The codes all solve the Navier–Stokes equations but differ in implementation, grid type, and numerical methods. The focus of this paper will be on the comparison of the CFD codes to a recent wind-tunnel test that was designed primarily for CFD validation. The experiment was conducted by the NASA Exploration Technology Development Program in the Langley supersonic 4 × 4 foot Unitary Plan Wind Tunnel (LRC UPWT) in July 2010 [13,14]. The cases that will be presented all have a freestream Mach number of 4.6 and a Reynolds number of 1.5×10^6 per foot, but vary by the number of nozzles (0, 1, 3, or 4 nozzles), thrust coefficient ($C_T = T/qA_{\text{ref}} = 2, 3$), angle of attack (0, 12, 16, and 20 deg), and roll angle (0 and 180 deg). Time-accurate CFD simulations were conducted due to the inherent unsteadiness of the flowfields.

Qualitative comparisons of the flow structure will be made by comparing CFD to high-speed Schlieren images, and quantitative comparisons will be made by comparing time-averaged surface pressure with pressure tap data from the tunnel. Unsteady shedding frequencies of the CFD solutions can be compared to high-frequency pressure gauges from the test. This effort is still underway, but some results can be seen in [15].

Presented as Paper 2012-0864 at the AIAA 50th Aerospace Sciences Meeting, Nashville, TN, 9–12 January 2012; received 24 April 2013; revision received 16 October 2013; accepted for publication 21 October 2013; published online 3 April 2014.

*Aerospace Engineer, Jacobs Technology, Applied Aeroscience and CFD Branch, EG3. Member AIAA.
†Research Scientist, Aerothermodynamics Branch, MS 230-2. Senior Member AIAA.
‡Aerospace Engineer, Aerothermodynamics Branch, MS 408A. Lifetime Member AIAA.
§Aerospace Engineer, Computational Aero-Sciences Branch, MS 128. Senior Member AIAA.
¶Aerospace Engineer, Atmospheric Flight and Entry Systems Branch, MS 489. Senior Member AIAA.

This paper will first introduce SRP, the CFD codes, and the wind-tunnel test. Then it will present code-to-code and code-to-test comparisons as well as a discussion of the results including modeling strengths and weaknesses and then offer conclusions of the study.

II. Supersonic Retropropulsion Flow Structure

Figure 1 shows a representative wind-tunnel model that employs SRP along with the resulting flowfield. The vehicle is a sphere cone with a single nozzle in the center and a sting for mounting it in the tunnel. In supersonic flow, a bow shock forms. As an opposing jet is initiated, the bow shock is pushed upstream as the apparent body frontal area is increased with the appearance of a barrel plume. The barrel plume contains free shear layers as well as a terminal shock. Between the terminal and bow shocks is an interface or contact surface where opposing velocities stagnate. With the barrel plume, recirculation regions appear as well as a triple point, where it can be said that three types of flow meet: supersonic jet flow, subsonic shock-layer flow, and subsonic recirculating flow.

The previous description is an example of a single jet flow at a relatively high thrust coefficient. Other modes exist depending on jet-to-freestream pressure ratios, including a long-jet penetration mode at low ratios. With multiple nozzles, interaction between barrel plumes may also exist, and the apparent body frontal area can change depending on the location of the nozzle on the model face and orientation angle of the nozzles [16,17].

III. Description of Computational Fluid Dynamics Solvers

The three solvers applied to the SRP problem differ in implementation, grid type, and numerical methods. DPLR and FUN3D are finite-volume, while OVERFLOW is finite-difference. DPLR uses cell-centered structured overset grids, while OVERFLOW uses node-centered structured overset grids. FUN3D employs node–centered unstructured grids. With these differences between codes, much is to be learned through code-to-code comparison when applying them to a single set of problems.

This paper builds from [15], which focuses on a single run of the LRC UPWT test. In [15], an in-depth look at grid and time resolution and convergence, observed order of accuracy, turbulence models, and the establishment of best practices is described in detail. The following are brief descriptions of each code including the numerical methods used by each in this study.

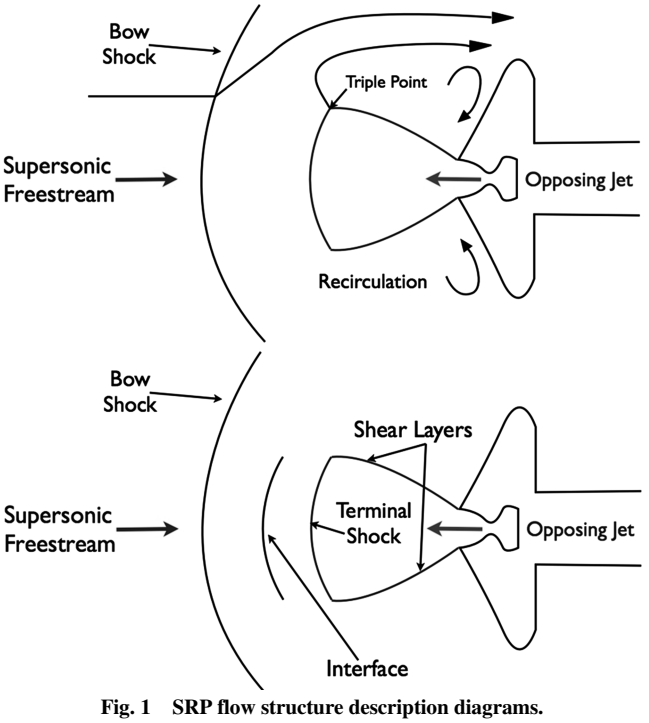

Fig. 1 SRP flow structure description diagrams.

A. DPLR

The DPLR CFD code is a parallel, structured multiblock, finite-volume code with overset grid capability that solves the Reynolds-averaged Navier–Stokes (RANS) equations for continuum flow, including finite-rate chemistry and thermal nonequilibrium. In the present study, the thermally and calorically perfect RANS equations for air are solved implicitly with first-order time accuracy. Inviscid fluxes are formed via a modified Steger–Warming flux vector splitting [18] with third-order monotone upwind scheme for conservation laws (MUSCL) extrapolation [19] subject to a minmod limiter [20] and second-order flux integration. The viscous terms are computed with second-order spatial accuracy with a central difference approach. For the present analysis, the Menter's shear-stress transport (SST) turbulence model [21] was employed with a vorticity-based production term and no compressibility corrections.

B. FUN3D

FUN3D contains a node-based finite-volume unstructured flow solver. For this study, FUN3D was run with a selectively dissipative version of the low-dissipation flux splitting scheme inviscid flux function [22] and a modified van Albada et al. [23] limiter according to Vatsa and White [24] and White [25]. Detached-eddy simulation (DES) turbulence modeling was used with Spalart–Allmaras (SA) [26] as the submodel. The zero-nozzle cases were completed with the compressible RANS equations loosely coupled to Menter's SST turbulence model with a vorticity-based production term. Node-based conservative variables are computed by driving a second-order accurate spatial residual to steady state with a point-implicit iterative method. A modified, optimum second-order backward difference formula scheme is used in conjunction with a temporal error controller that assured design order [27].

C. OVERFLOW

OVERFLOW 2 is an implicit Navier–Stokes flow solver that uses structured overset grids. For the current work, the HLLE++ numerical flux function [28] with the van Albada limiter was used for spatial terms, and the symmetric successive overrelaxation algorithm with dual time stepping using Newton subiterations for temporal terms. All viscous terms were included, and the SST turbulence model with strain-based production was employed with Wilcox's realizability constraint [29]. The overall scheme is second-order accurate in space and time. The calculation of the inviscid fluxes for both the flow solver and the turbulence model use third-order accurate MUSCL reconstruction and second-order flux quadrature. For the single and three-nozzle configurations, DES turbulence modeling with SST as the submodel was used; and for the zero- and four-nozzle configurations, RANS SST turbulence modeling was used for solution stability.

IV. Supersonic Retropropulsion Wind-Tunnel Test

Test 1853 in the LRC UPWT was designed specifically for SRP CFD validation. The model was a 70 deg sphere–cone forebody with a cylindrical side body 5 in. in diameter. The model included four nozzles, which could be plugged to offer a zero-, one-, three-, or four-nozzle configuration. One nozzle was located at the center of the forebody, and the three others were oriented radially every 120 deg at $1/2$ radius. Air was used as both the freestream and jet gases. The test data included high-speed Schlieren movies and pressure readings from 167 taps including seven 40 kHz pressure transducers. From these data, qualitative comparisons with CFD flow structure and unsteady behavior can be made with the Schlieren movies, as well as averaged surface pressure comparisons with the pressure taps.

The test run matrix included four nozzle configurations: zero, one (center), three (peripheral), and four (center and peripheral). Three Mach numbers were tested: 2.4, 3.5, and 4.6. The Re/ft for the two lower Mach numbers was 1.0×10^6, and for Mach 4.6, Re/ft was

1.5×10^6. Thrust coefficients ranged from 0.5 to 3, with isolated runs up to 6. To avoid liquefaction, the jet air supply was heated to 150°F. Angles of attack swept from −8 to 20 deg. A full description of the test can be found in reference [13]. Figure 2 is a snapshot of the model in the three-nozzle configuration in the test section. Figure 3 shows diagrams of the model face and side-body pressure tap layouts [30]. The filled circles represent the high-frequency Kulite® pressure transducers. The figure represents 172 planned pressure taps including nine 40 kHz pressure transducers; the final count was 167 taps with seven 40 kHz pressure transducers. Pressure taps were only placed on half of the model side due to symmetry.

Wind-tunnel uncertainty was calculated using an entirely statistical approach based on comparing multiple measurements of surface pressure coefficient in a specially designed sampling technique [30]. The uncertainty contains contributions from random sources (instrumentation drift, hysteresis, etc), flowfield nonuniformity, and model geometry and instrumentation uncertainties. The final pressure coefficient uncertainty for Mach 4.6 is shown in Table 1, where it is seen that flowfield nonuniformity is the largest contributor. This is the same trend seen in the seminal use of this uncertainty quantification technique [31]. For the CFD comparisons, three times the standard deviation was applied about the average surface pressure coefficient ($\pm 3\sigma$).

The uncertainty analysis was conducted on the baseline (no jet) configuration. As such, it does not include contributions introduced by the jets or the unsteadiness in the plumes. Although these contributions cannot be quantified directly, scatter in the results of repeated blowing cases were largely contained within 3σ certainty limits [30].

Fig. 2 SRP test model in the three-nozzle configuration in the NASA LRC UPWT test section 2.

Table 1 Pressure measurement uncertainty contributions for Mach 4.6 conditions

Source	σ	Percent total
Random	0.00294	15
Flowfield	0.00637	71
Geometry	0.00276	13
Total	0.00754	100

V. Results

A total of 18 cases were simulated with the CFD solvers. They focused on the highest Mach number (4.6) to decrease the probability of wall interference in the tunnel, which had large boundary layers in the test section. The cases vary in angle of attack, roll angle, thrust level, and the number of nozzles (see Table 2). Reynolds number per foot was 1.5×10^6, and freestream static temperature was 116.6°R.

Images of the grids used for each code are shown in Fig. 4. Each grid has a different topology, but all focus refinement in the shock interaction region. A more thorough description of grid refinement studies and final grid spacings is found in reference [15]. No grid adaptation was used for the blowing cases.

Comparisons of results between the three CFD flow solvers and the wind-tunnel data are shown in Figs. 5–30. The plot designs will be described next, and a full discussion of the results will be presented later.

The black and white images labeled as "TEST" are instantaneous images gathered from the high-speed Schlieren system from the LRC UPWT test. The black columns in the images are the structural bars across the viewing window of the wind tunnel. CFD flow visualizations for run 283 are Mach number contours in grayscale. For all blowing cases, the CFD solvers show grayscaled surface pressure coefficient on the model. For run 165, the DPLR flowfield is shown through grayscaled Mach number contours on the symmetry plane, and the OVERFLOW flowfield is shown through grayscaled contours of the log of the density gradient magnitude on the symmetry plane. For all other blowing cases, the computed flowfield from the CFD solvers is visualized through constructed Schlieren or shadowgraph representations generated through volume integration as described by Yates [32]. All flowfield visualizations regardless of the method were meant to represent the shock structure in a comparable way to the test Schlieren. To account for $\phi = 180$ deg rotations, negative angles of attack were used for the FUN3D results.

Columns in the flow visualizations montages are snapshots in time (labeled Time 1, Time 2, Time 3, and Time 4), but are not consistent between the CFD simulations or test Schlieren due to the aperiodic nature of all but some of the run 165 cases, and the differences in time

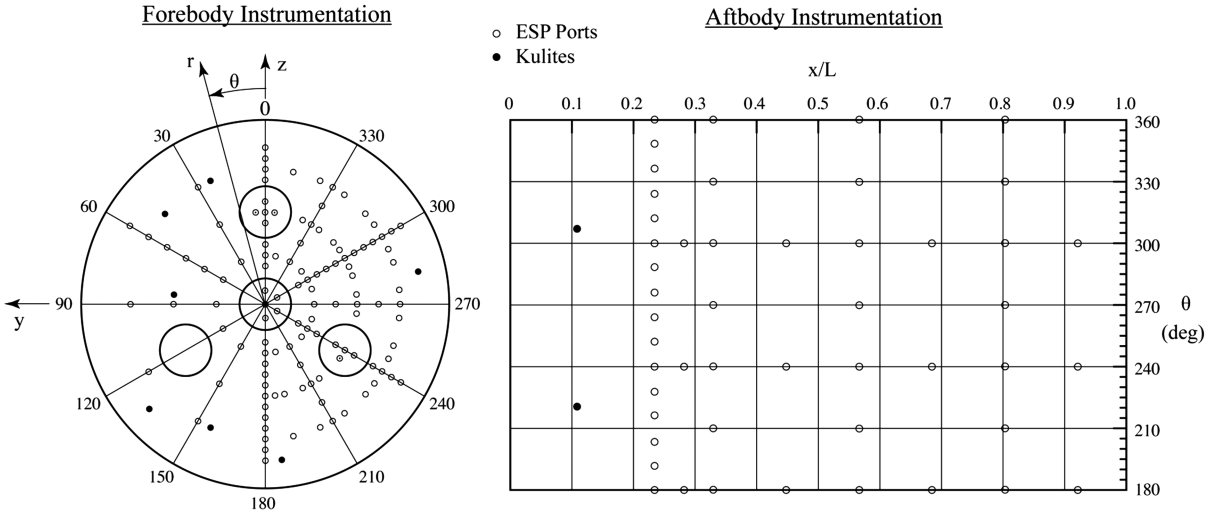

Fig. 3 Pressure tap layout on test model face (left) and side body (right).

Table 2 CFD run matrix

Run number	Nozzles	C_T	$P_{o,\text{jet}}$, psia	$T_{o,\text{jet}}$, °R	Angles of attack α, deg	Roll angle ϕ, deg
283	0	N/A	N/A	N/A	0, 12, 20	0
165	1	2	598.9	622.1	0, 12, 20	180
262	3	3	302.8	624.1	0, 12, 16	0
263	3	3	303.1	630.9	0, 12, 16	180
307	4	2	151.9	618.2	0, 12, 20	0
311	4	2	152.4	620.7	0, 12, 20	180

steps used by each code. Each point in time was chosen to best represent the behavior observed in the flowfield.

In the line plots, comparisons between the codes and experimental values of the averaged surface C_P are shown using two coordinate systems. The first shows pressures on the model face in radial coordinates normalized by the model radius. Data from both $\theta = 0$ deg and $\theta = 180$ deg (see Fig. 3) are shown on the same plot. The second set of plots show pressure coefficients along the body axis as a function of X/L. The shaded regions are the model surface where the pressure coefficient is being plotted; the surface is slightly transparent to reveal the location of the embedded nozzles.

Forces and moments as a function of time are also plotted as a code-to-code comparison. The test did not include a balance, and an integration of the pressure tap values only yields averaged aerodynamic loads. Total axial force is plotted, which is a summation of the aerodynamic and thrust components to axial force. Through these plots, it is possible to compare the level of unsteadiness between the codes as well as gain an understanding of how much the unsteadiness may influence the stability of a vehicle at these conditions. The ranges for the axes were chosen to best represent the detail captured by each code. As such, the ranges are not the same between cases, and careful attention is required when comparing. The force and moment integration was conducted on the model face and side; it did not include the model base. The reference length and area used in nondimensionalizing the coefficients are $L_{\text{ref}} = 5.0$ in. and $A_{\text{ref}} = 19.63$ in^2; the reference length is the diameter of the model, and the reference area is the projected frontal area. The moment reference center was at the nose of the model, or where the nose of the model would be when the center plug was removed. The time period shown in the plots do not represent the total run time of the CFD codes but was based on the code that was run for the smallest amount of time.

A. Run 283: Zero-Nozzle

Run 283 is a baseline, zero-nozzle case resulting in a steady supersonic blunt-body flow, which is simpler than the powered cases. As shown in Figs. 5 and 6, each code compared well to each other and to the test in shock standoff distances and surface C_P. The DPLR visualizations shown in Fig. 5 depict very little flowfield upstream of the bow shock, which demonstrates the bow shock grid adaptation feature in the DPLR code. The wake region of the FUN3D simulations are more smeared than the other codes due to a relatively coarse grid in that area.

Overall, the CFD codes predict higher pressure on the model face than the experiment (Fig. 6), but still generally within the error bars. However, the pressure at the nose is an area of deviation between the CFD codes and the test data for $\alpha = 12$ deg and $\alpha = 20$ deg with the CFD codes all overpredicting. The Rayleigh pitot formula gives the maximum C_P for Mach 4.6 flow to be 1.80, which correlates to the C_P at the nose for $\alpha = 0$ deg. For $\alpha = 0$ deg, the test data (1.78) results show a slightly lower value than 1.80 while the DPLR (1.81), FUN3D (1.80), and OVERFLOW (1.79) results are closer to the

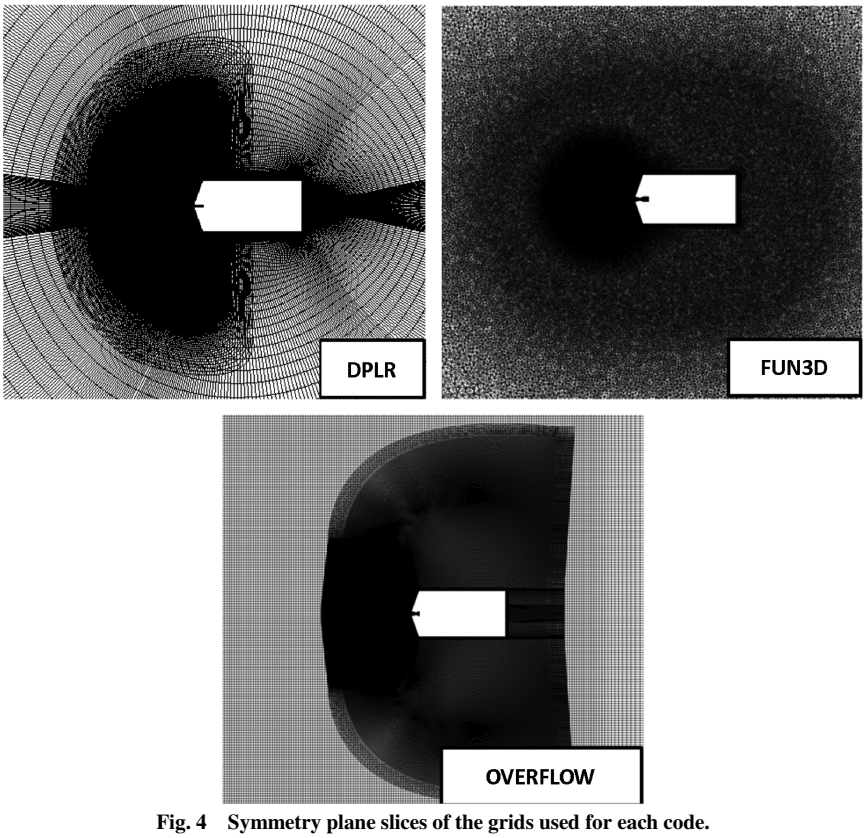

Fig. 4 Symmetry plane slices of the grids used for each code.

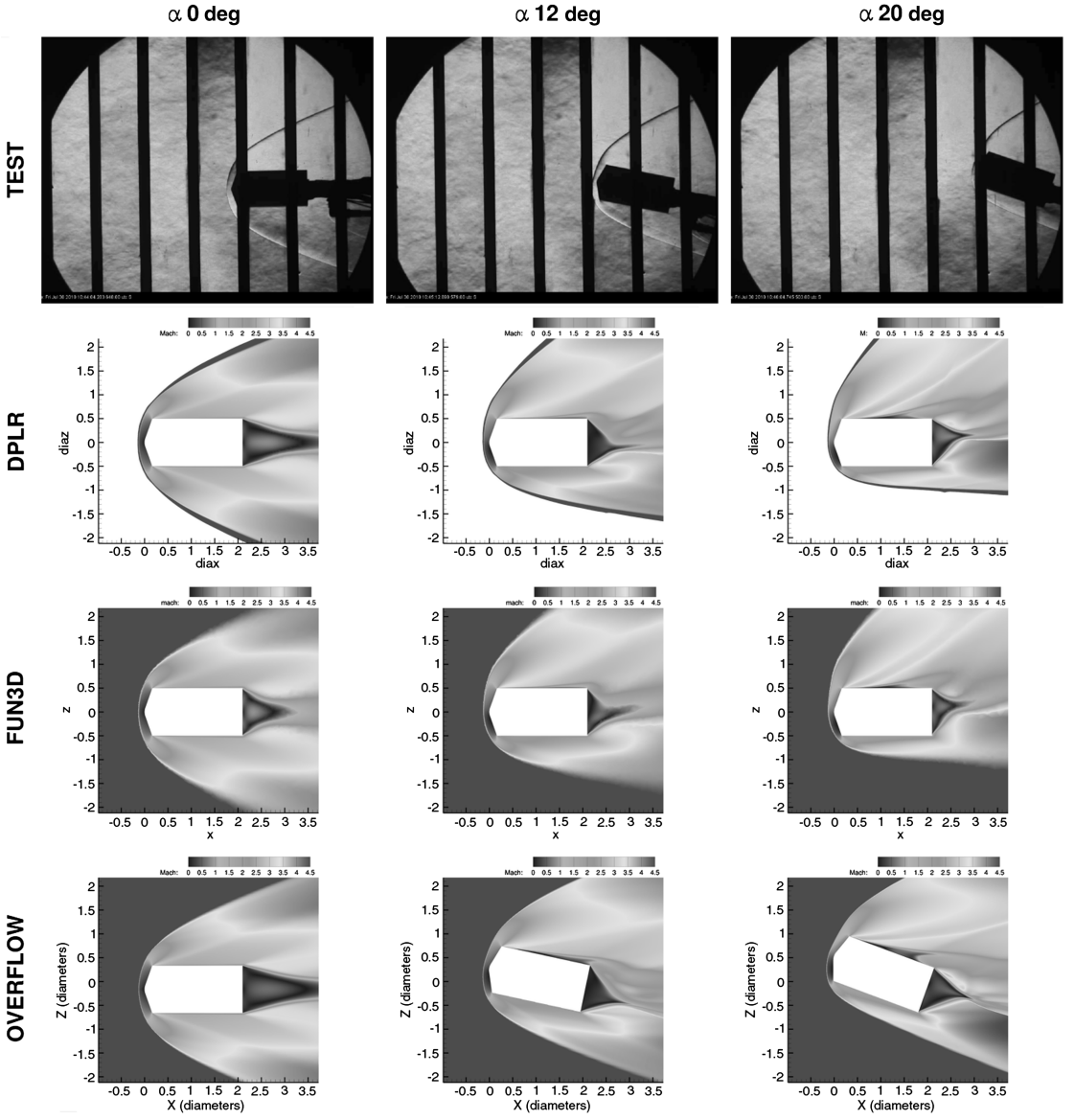

Fig. 5 Flow visualizations of run 283: baseline, zero-nozzle.

theoretical value. This may show that the test data are biased slightly low, likely due to flow nonuniformity in the tunnel. This causes a deviation at the nose for $\alpha = 0$ deg that is within the uncertainty bars but may cause larger deviations at the nonzero angles of attack.

B. Run 165: One-Nozzle, $C_T = 2$

Run 165 $\alpha = 0$ deg was used to establish the best practices for each code [15]. It was chosen because of its periodic unsteadiness, which simplified comparisons. The unsteadiness can be described as an oscillation of the triple point (described three-dimensionally as an annular ring), which creates pressure waves that propagate up to the bow shock causing a minimal effect and propagate to the model. The waves reflect off the model face and in turn off the barrel plume shear layers, which causes another oscillation of the triple point. Visualizations of the single nozzle cases at varying angles of attack are seen in Figs. 7–9.

Each code captured this unsteadiness to a different degree, the differences in turbulence modeling and grid refinement appear to be the key contributors to the deviations as shown in reference [15]. The level of unsteadiness can be seen in the force and moment plots in Fig. 10, where OVERFLOW and FUN3D have larger oscillation amplitudes than DPLR, and the DPLR case trends toward a steady solution.

An effect of capturing the described unsteady effects can be noted in the model face surface C_P for $\alpha = 0$ deg seen in Fig. 10. The codes that captured the unsteadiness captured the pressure wave as it reflected off the model face, and in turn, a higher averaged pressure near the nozzle was predicted. This trend is also seen in the wind-tunnel data. However, the tunnel uncertainties are large enough to envelope the CFD data that did not capture the unsteady effects.

For $\alpha = 12$ deg, the flow unsteadiness becomes less periodic. A shedding from the windward side of the triple point occurred, which was again captured to different degrees between the codes. More deviation between the codes and test is seen in the C_P plots. All codes predict pressures on the side body within test uncertainties, but only OVERFLOW does for the complete model face. More deviation on the windward side of the face is seen, especially near the shoulder ($r/R = 1.0$). FUN3D overpredicts pressure near the shoulder, while DPLR underpredicts.

For $\alpha = 20$ deg, the flow unsteadiness becomes aperiodic. Large shedding occurs randomly, and a large run time was required to obtain meaningful averages from the CFD cases. The CFD results mostly fall inside the tunnel uncertainty for averaged surface C_P even though different behaviors are seen in the simulations. The DPLR results appear to have a periodic unsteadiness in the force and

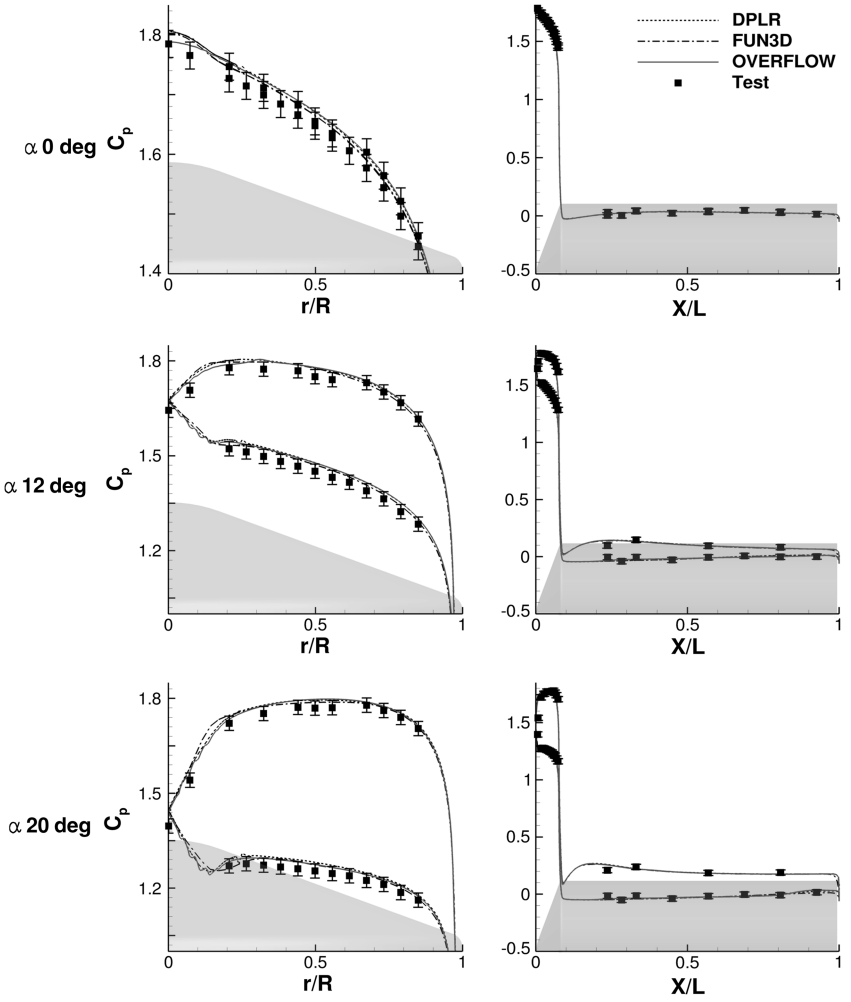

Fig. 6 Pressure coefficient on the model surface for run 283: baseline, zero-nozzle.

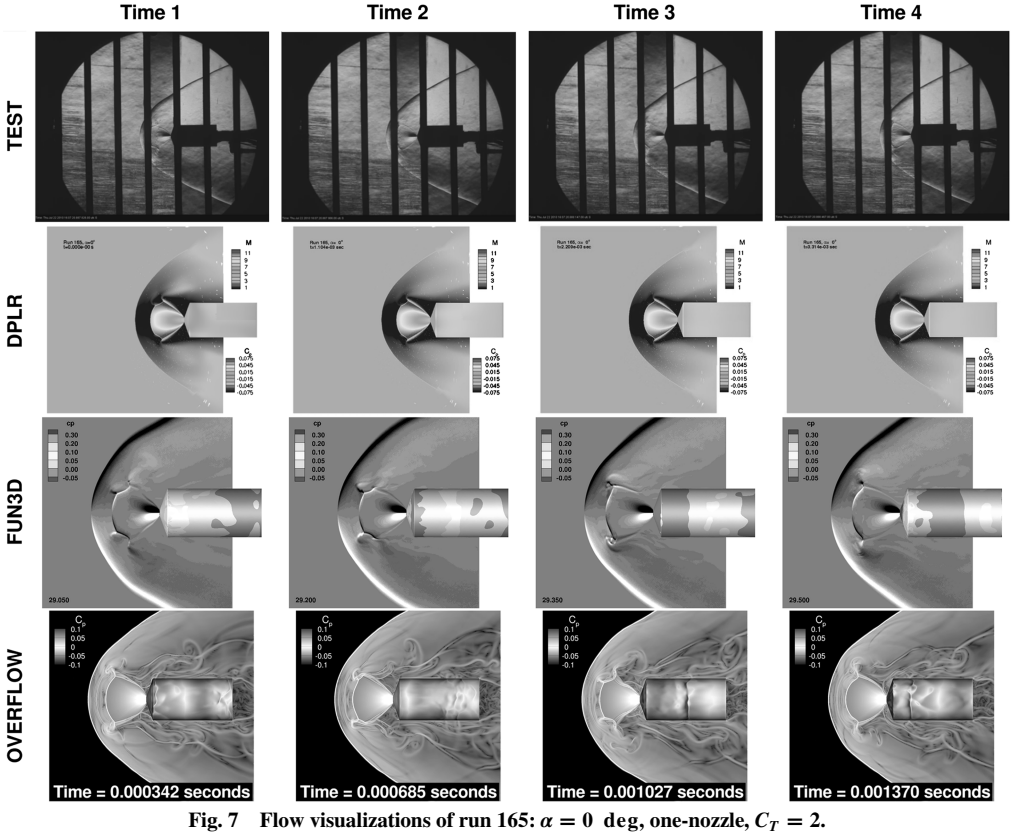

Fig. 7 Flow visualizations of run 165: $\alpha = 0$ deg, one-nozzle, $C_T = 2$.

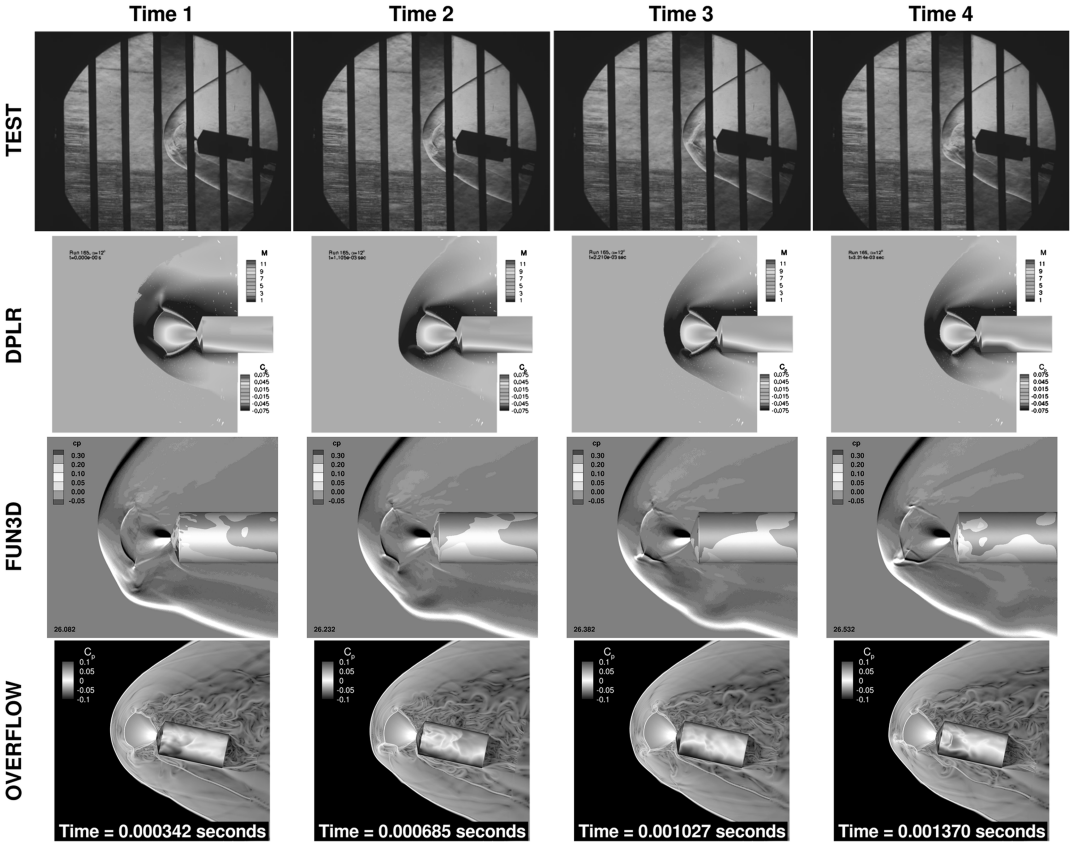

Fig. 8 Flow visualizations of run 165: $\alpha = 12$ deg, one-nozzle, $C_T = 2$.

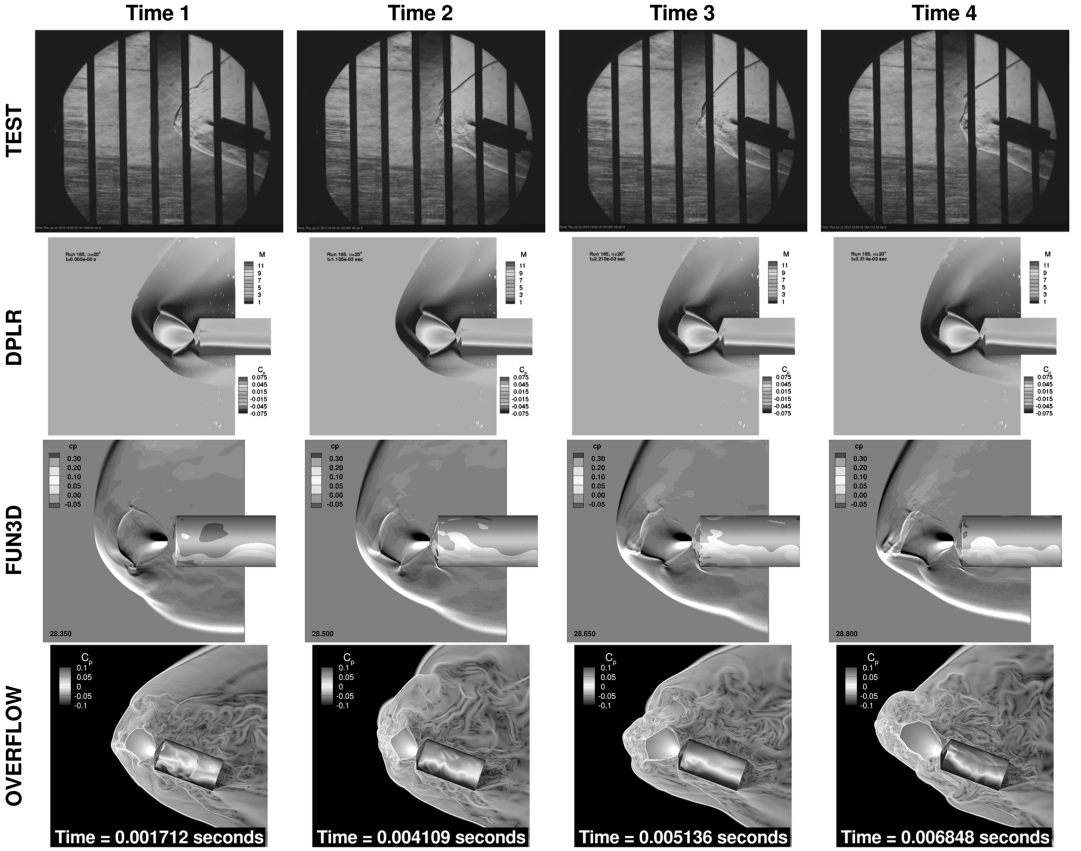

Fig. 9 Flow visualizations of run 165: $\alpha = 20$ deg, one-nozzle, $C_T = 2$.

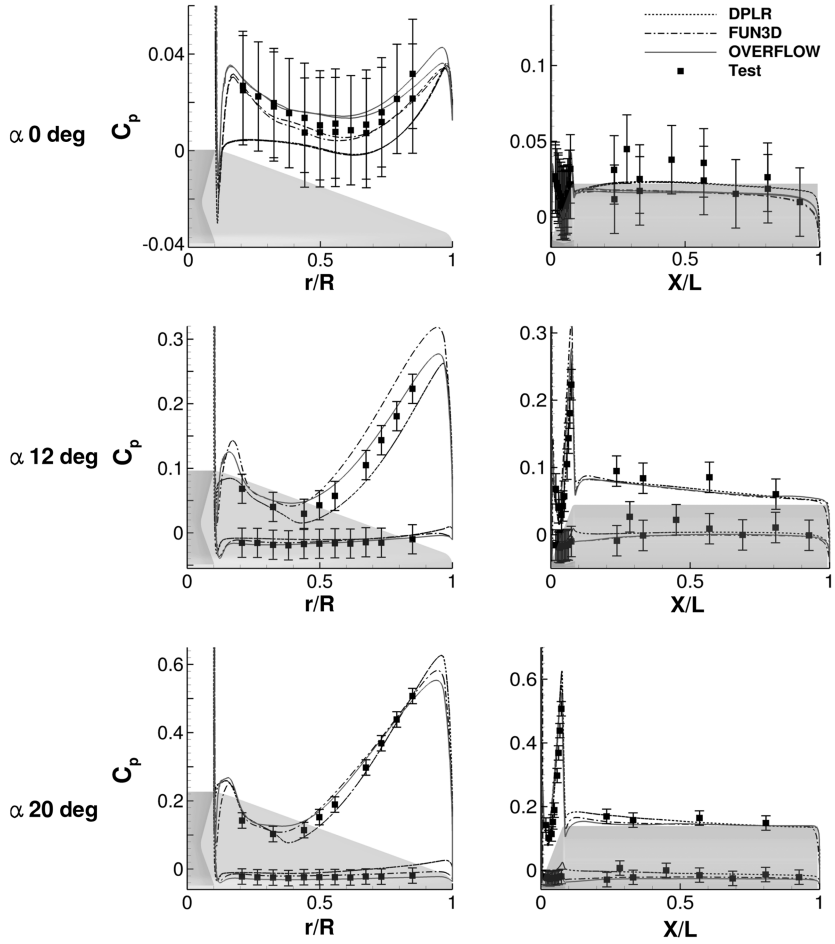

a) Comparison of time-averaged surface C_P

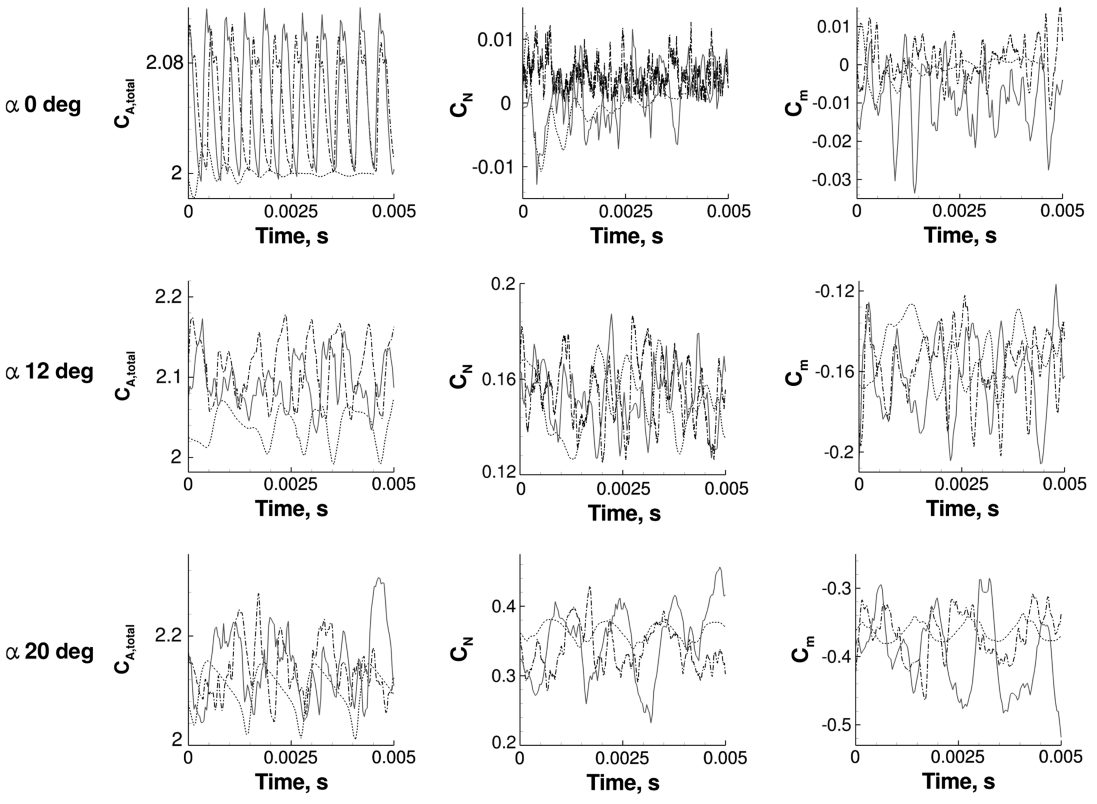

b) Code-to-code comparison of $C_{A,\text{total}}$, C_N, and C_m

Fig. 10 Comparisons of a) surface C_P, and b) $C_{A,\text{total}}$, C_N, and C_m as a function of time for run 165: one-nozzle, $C_T = 2$. Both Figs. 10a and 10b share the same line legend, the same for Figs. 15, 20, 25, and 30.

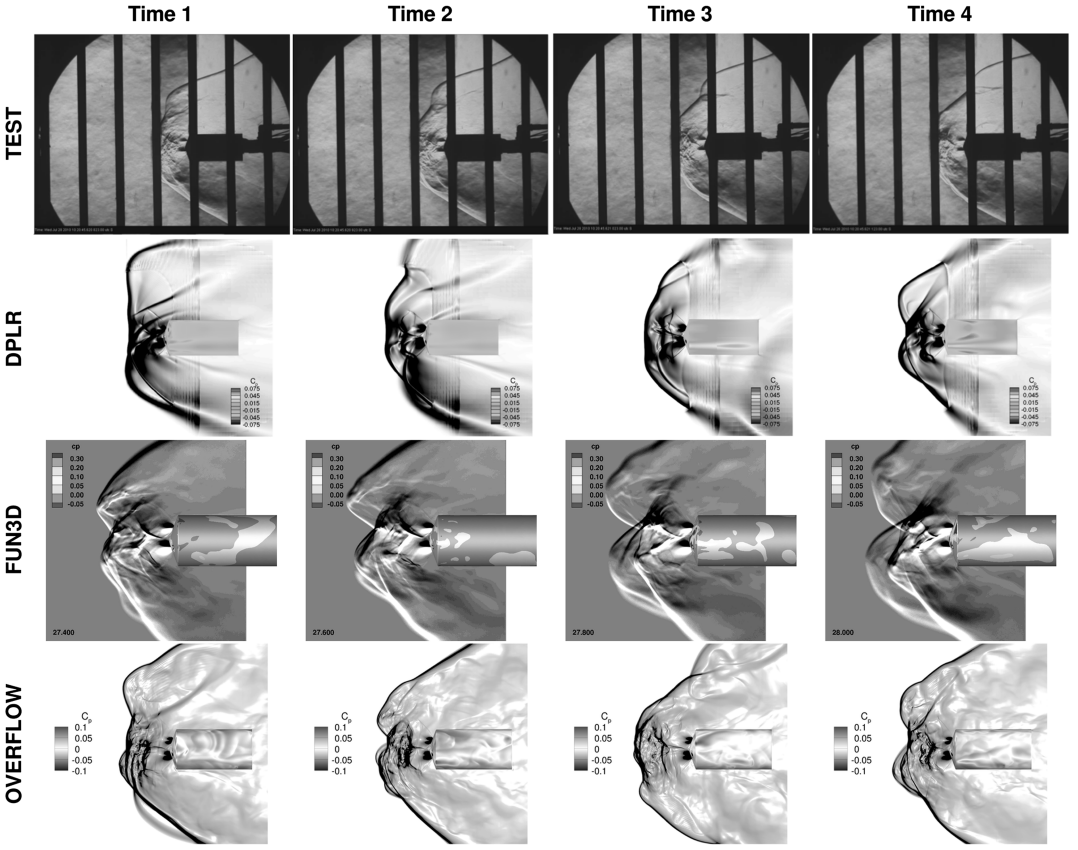

Fig. 11 Flow visualizations of run 262: $\alpha = 0$ deg, $\phi = 0$ deg, three-nozzle, $C_T = 3$.

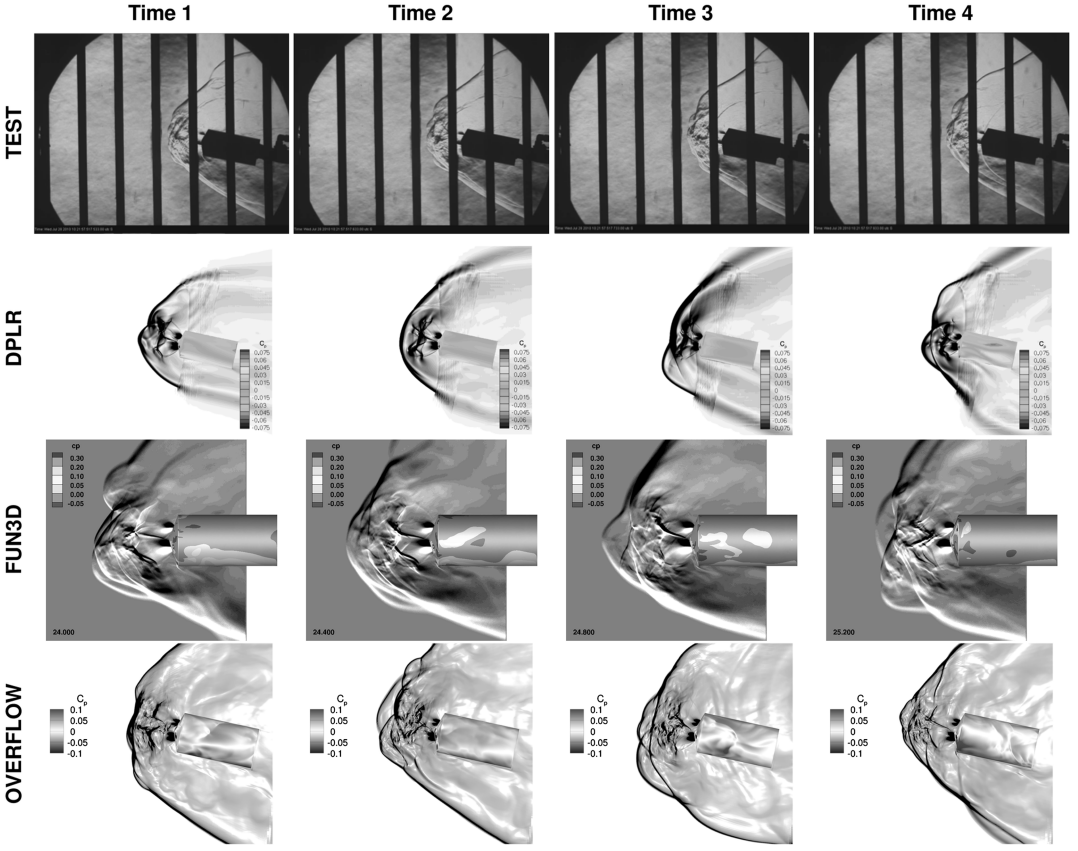

Fig. 12 Flow visualizations of run 262: $\alpha = 12$ deg, $\phi = 0$ deg, three-nozzle, $C_T = 3$.

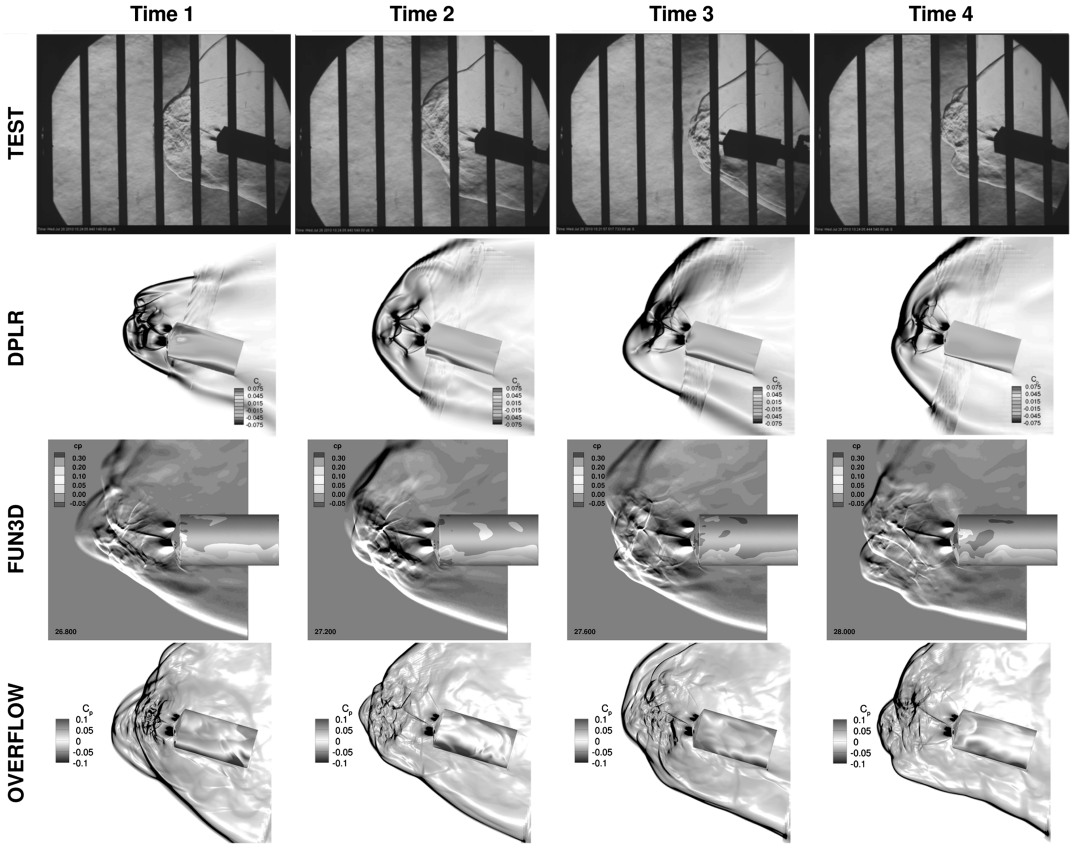

Fig. 13 Flow visualizations of run 262: $\alpha = 16$ deg, $\phi = 0$ deg, three-nozzle, $C_T = 3$.

moment plots, while the OVERFLOW and FUN3D results show a more aperiodic behavior.

C. Run 262: Three-Nozzle, $C_T = 3, \phi = 0\,deg$

Run 262 displayed aperiodic behavior in the plume/freestream interaction region (Figs. 11–13, close-up of OVERFLOW simulation in Fig. 14). The unsteadiness was shown in the bow shock behavior, which oscillated to different degrees throughout the testing time window. Qualitatively, the FUN3D and OVERFLOW results most resemble the test Schlieren; however, that did not guarantee a good comparison to average surface pressure (Fig. 15). In the DPLR simulated shadowgraph images, the skewness in the area just aft of the model shoulder is due to a drop in grid resolution in an overset region (see Fig. 4). This also causes spikes in the average surface coefficient plots on the model sidebody.

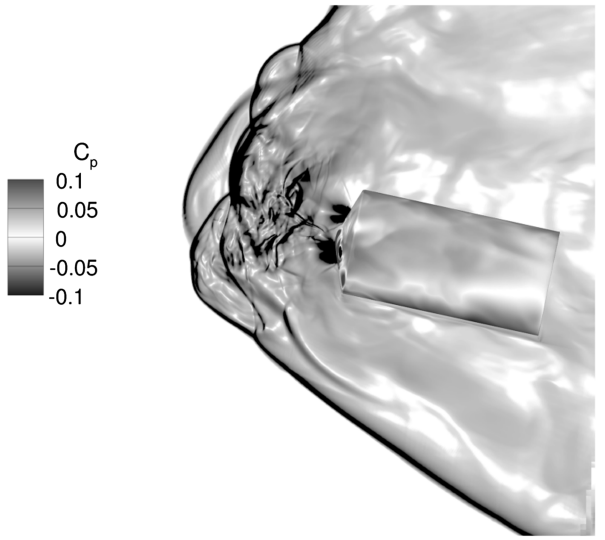

Fig. 14 Close-up OVERFLOW flow visualizations of run 262: $\alpha = 12$ deg, $\phi = 0$ deg, three-nozzle, $C_T = 3$.

The level of unsteadiness for each code is apparent in the force and moment plots seen in Fig. 15. Large deviation is seen in the total axial force between the codes. The thrust component of the coefficient overpowers the aerodynamic effects, and as such, small deviations in properly simulating the thrust coefficient become apparent. The computed C_T from the test was 2.94, which is closely simulated by FUN3D (2.99) and OVERFLOW (2.98), while DPLR simulated a larger C_T (3.11).

For the surface pressure in Fig. 15, large deviations between the codes are seen at the model nose. None of the codes properly predict the pressure at the nose for $\alpha = 0$ deg, OVERFLOW comes close for $\alpha = 12$ deg, and better agreement is seen for $\alpha = 16$ deg. Differences in simulated jet expansion and jet-to-jet interactions may be the source of these deviations.

For both $\alpha = 0$ deg and $\alpha = 12$ deg, FUN3D overpredicts the pressure for $r/R < 0.4$ and for the entire model face for $\alpha = 12$ deg. The rise in pressure near the nozzle at $r/R \sim 0.35$ is captured in behavior and value by OVERFLOW and in behavior for FUN3D. Large differences are seen on the windward side of the model face near the shoulder at nonzero angles of attack. In that region, DPLR and FUN3D properly predict the pressure for $\alpha = 16$ deg, while OVERFLOW overpredicts the pressure. At $\alpha = 12$ deg, a different trend is seen with OVERFLOW giving the best prediction of the three codes. On the model side-body, DPLR is consistently higher in average pressure than FUN3D and OVERFLOW with varying levels of agreement with tunnel data for all codes.

Given the unsteady nature of the flowfield, it is difficult to establish firm trends on the effects of turbulence modeling on jet expansion and jet interactions, but it is observed that the DPLR RANS results were more steady than the FUN3D and OVERFLOW DES results. Capturing more unsteadiness with DES modeling did not necessarily mean that the same effects measured by the wind tunnel test pressure ports were being modeled, as is demonstrated with the large differences in average C_P between FUN3D and OVERFLOW.

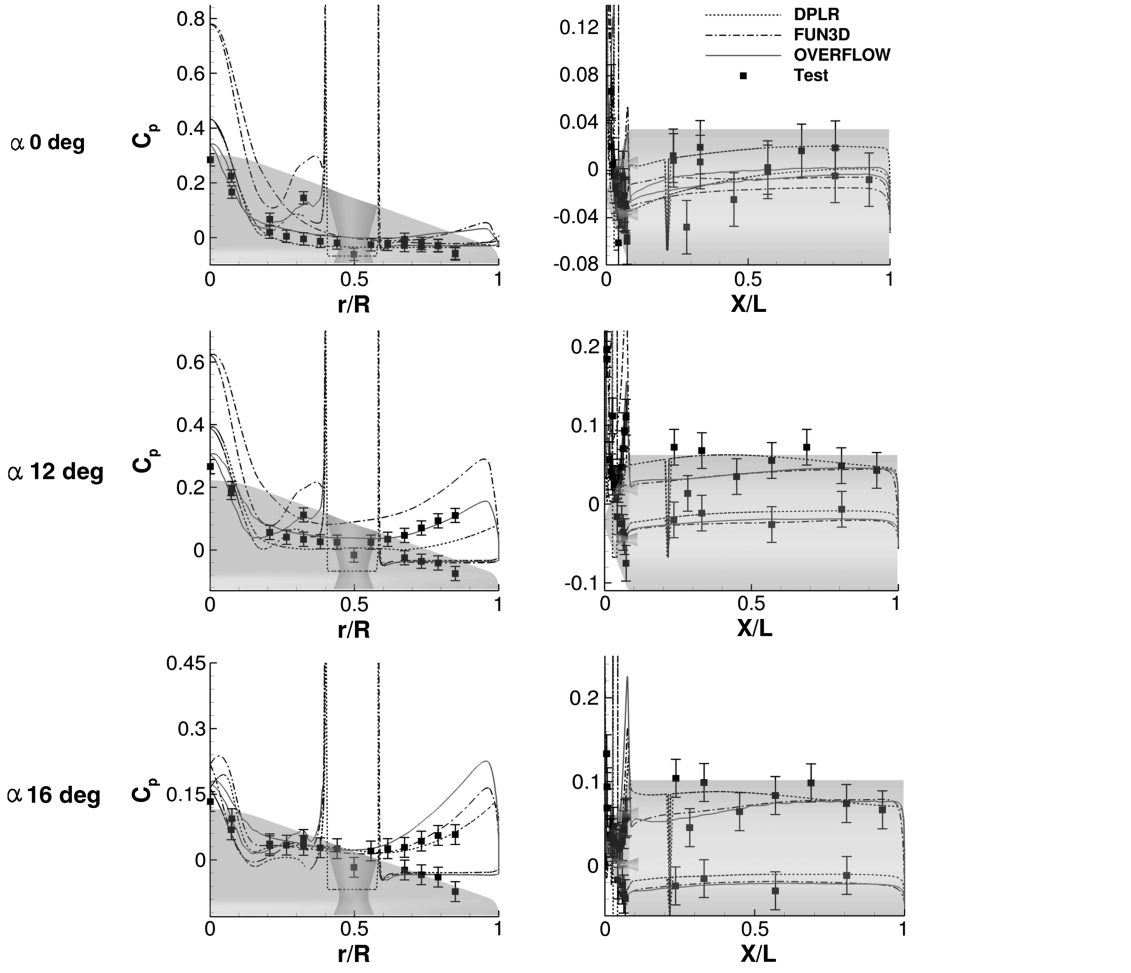

a) Comparison of time-averaged surface C_P

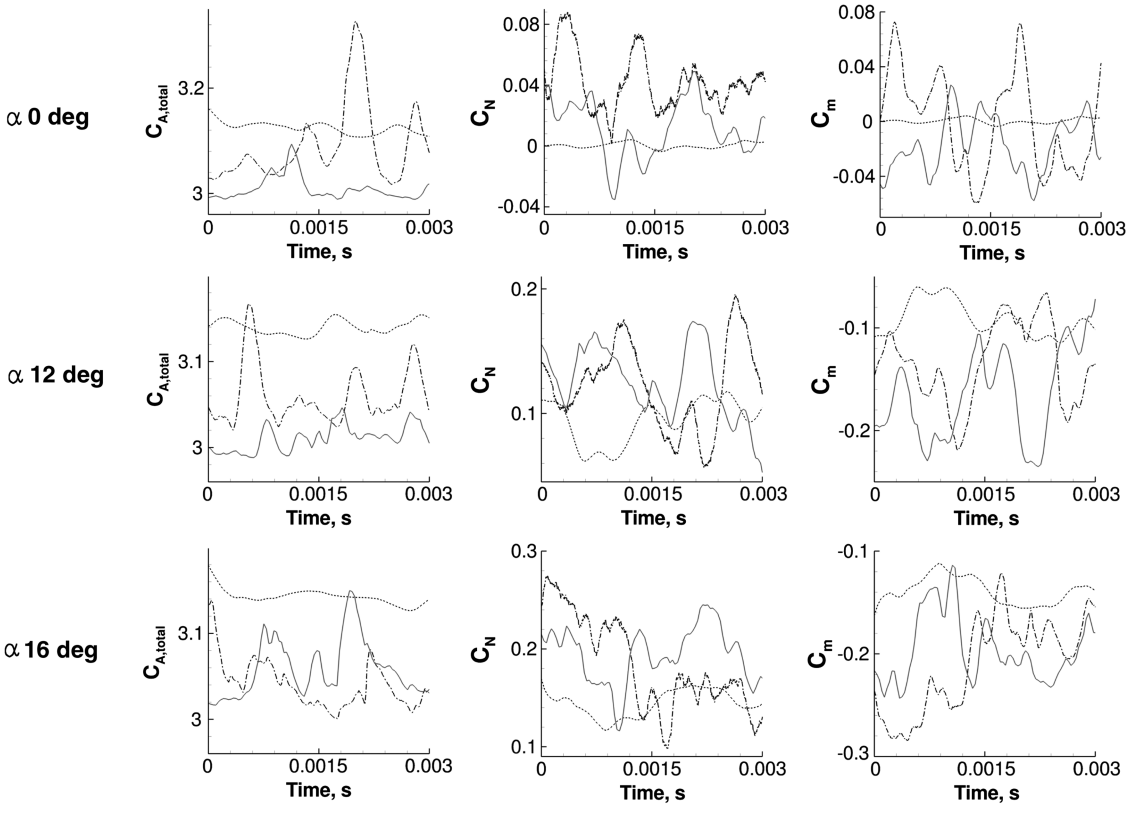

b) Code-to-code comparison of $C_{A,\text{total}}$, C_N, and C_m

Fig. 15 Comparison of a) surface C_P, and b) $C_{A,\text{total}}$, C_N, and C_m as a function of time for run 262: three-nozzle, $C_T = 3$, $\phi = 0$ deg.

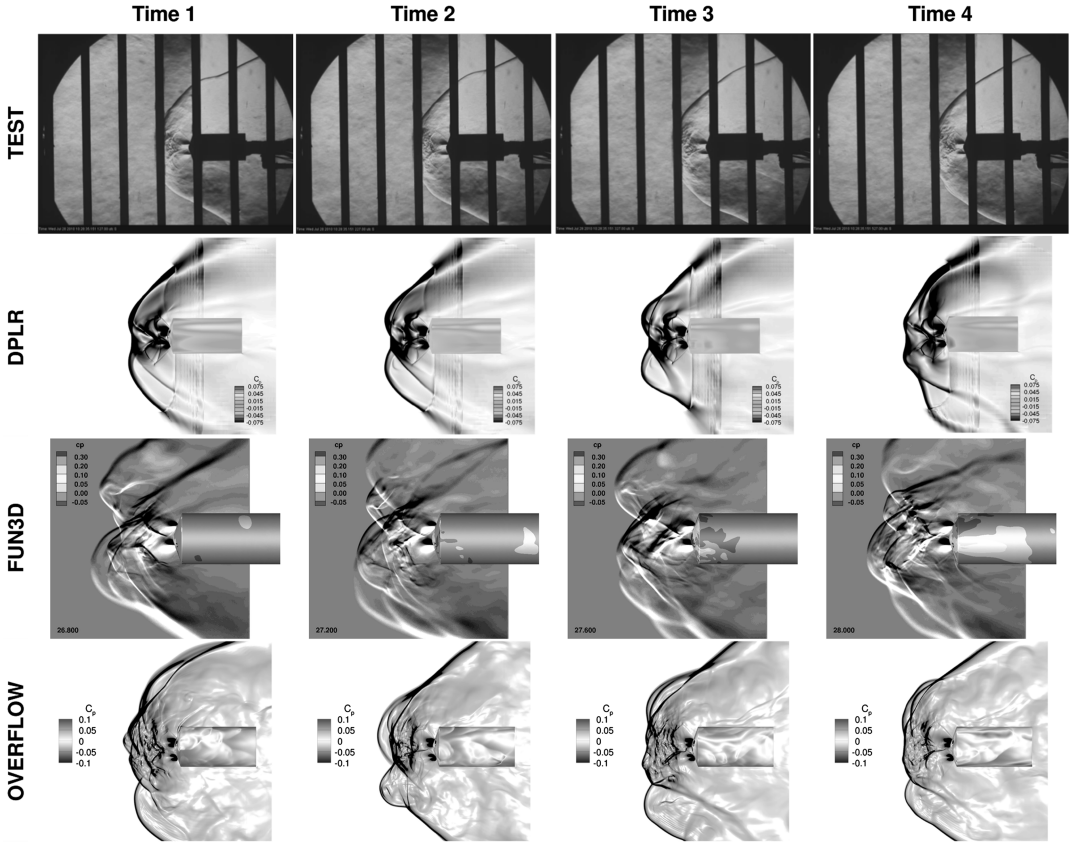

Fig. 16 Flow visualizations of run 263: $\alpha = 0$ deg, $\phi = 180$ deg, 3-nozzle, $C_T = 3$.

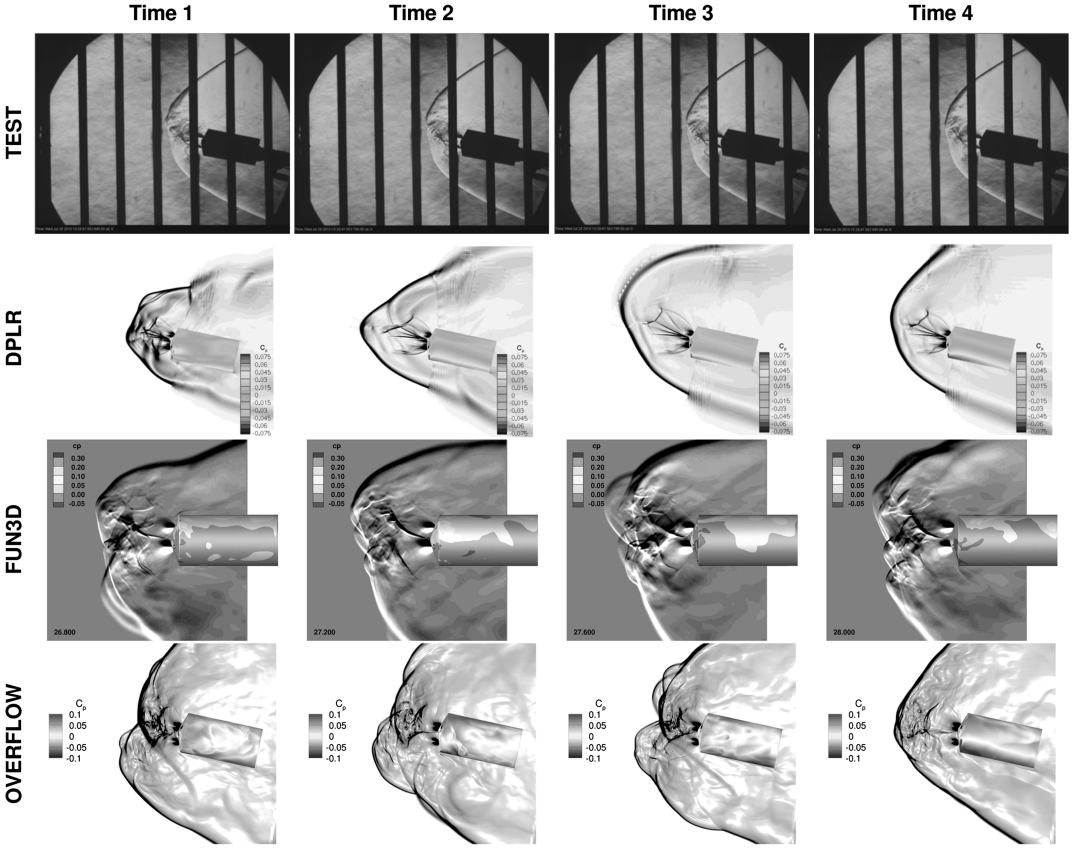

Fig. 17 Flow visualizations of run 263: $\alpha = 12$ deg, $\phi = 180$ deg, three-nozzle, $C_T = 3$.

D. Run 263: Three-Nozzle, $C_T = 3, \phi = 180 \times$ *Degrees*

Run 263 differs from run 262 only in roll angle. For positive-angle-of-attack cases, run 262 had a peripheral nozzle on the leeward symmetry plane of the forebody flank while run 263, which is rolled 180 deg, has this nozzle on the windward flank. Little difference from run 262 was seen or expected at $\alpha = 0$ deg (see Fig. 16). However, for $\alpha = 12$ deg and $\alpha = 16$ deg, run 263 displayed much steadier behavior than run 262, to the extent that the windward portion of the bow shock was essentially steady. This can be seen in Figs. 17–19. The windward side of the flowfield demonstrated a firmly placed bow shock, and little differences were seen in the barrel plume or termination shocks. Shedding from the jets did occur on the leeward side, which pushed the bow shock in that area back in a semi-oscillatory manner. The shedding was then pushed downstream, which for the most part did not affect the model surface.

The steadier flow behavior for nonzero angles of attack was captured the best by DPLR for $\alpha = 12$ deg and by FUN3D for $\alpha = 16$ deg.

In Fig. 20, pressure at the nose is again a weak point in the CFD simulations. Large deviation is seen between the codes, and all of the codes overpredict the tunnel data. The pressure on the model face for $\alpha = 0$ deg was overpredicted by FUN3D. For the nonzero angles of attack on the model side shell, the DPLR results compare the best with tunnel data on the windward side, while FUN3D and OVERFLOW underpredict for $\alpha = 12$ deg, and OVERFLOW underpredicts for $\alpha = 16$ deg.

E. Run 307: Four-Nozzle, $C_T = 2, \phi = 0 \times$ *Degrees*

Run 307 at $\alpha = 0$ deg (Fig. 21) demonstrated a steadier mode than seen in any of the three-nozzle cases (runs 262 and 263). The flow was similar to run 165 $\alpha = 0$ deg in that periodic oscillations of the triple points occurred, and the bow shock is in a steadier state relatively close to the body. However, the flow physics are more complex due to plume-to-plume interactions. For nonzero-angle-of-attack cases, similar unsteadiness to run 262 is observed.

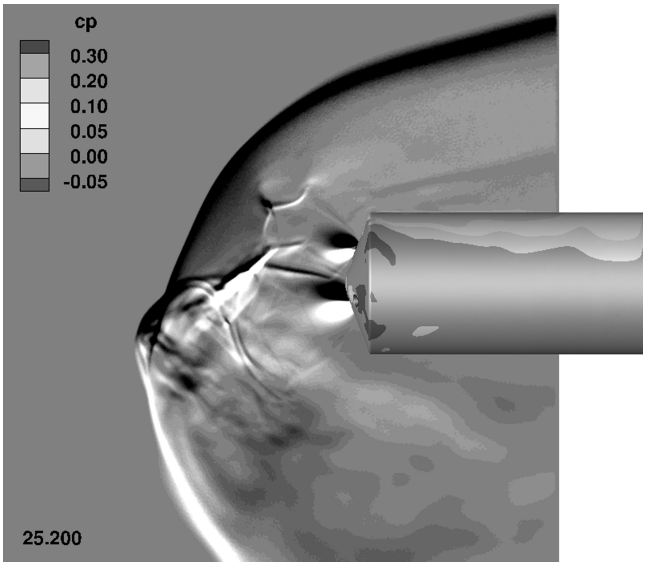

Fig. 19 Close-up FUN3D flow visualizations of run 263: $\alpha = 16$ deg, $\phi = 180$ deg, three-nozzle, $C_T = 3$.

For $\alpha = 0$ deg, FUN3D and OVERFLOW properly simulate the steadier flowfield with the reduced bow shock standoff distance. The DPLR simulation shows behavior of a larger bow shock standoff distance as it approaches a steady state. The bow shock standoff distance does not seem to influence the surface pressure because the plume structure is large enough to shield the model from freestream flow. The pressure on the model is relatively low, and all codes fall within experimental uncertainties with the exception of OVERFLOW below the center nozzle, see Fig. 25.

Compared to the zero-angle-of-attack case, all codes predict a higher level of unsteadiness for nonzero angles of attack, with FUN3D picking up the most fluctuations (Figs. 22–24). For the most

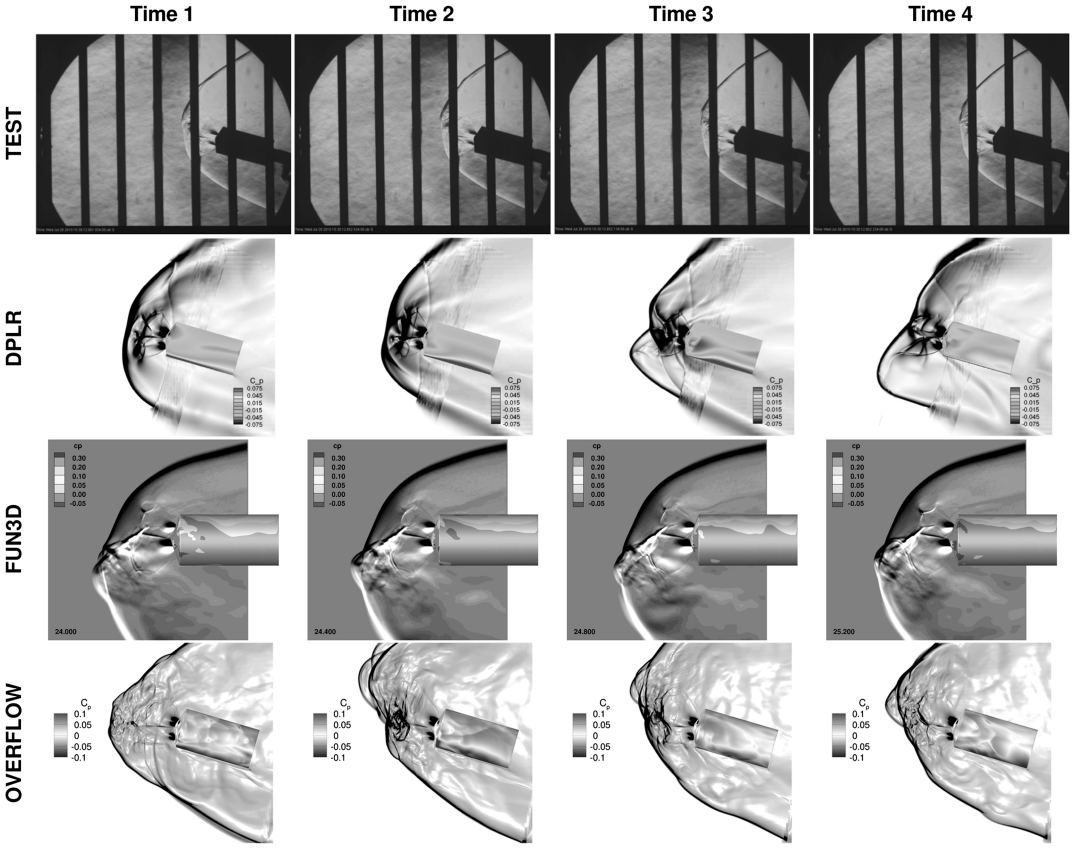

Fig. 18 Flow visualizations of run 263: $\alpha = 16$ deg, $\phi = 180$ deg, three-nozzle, $C_T = 3$.

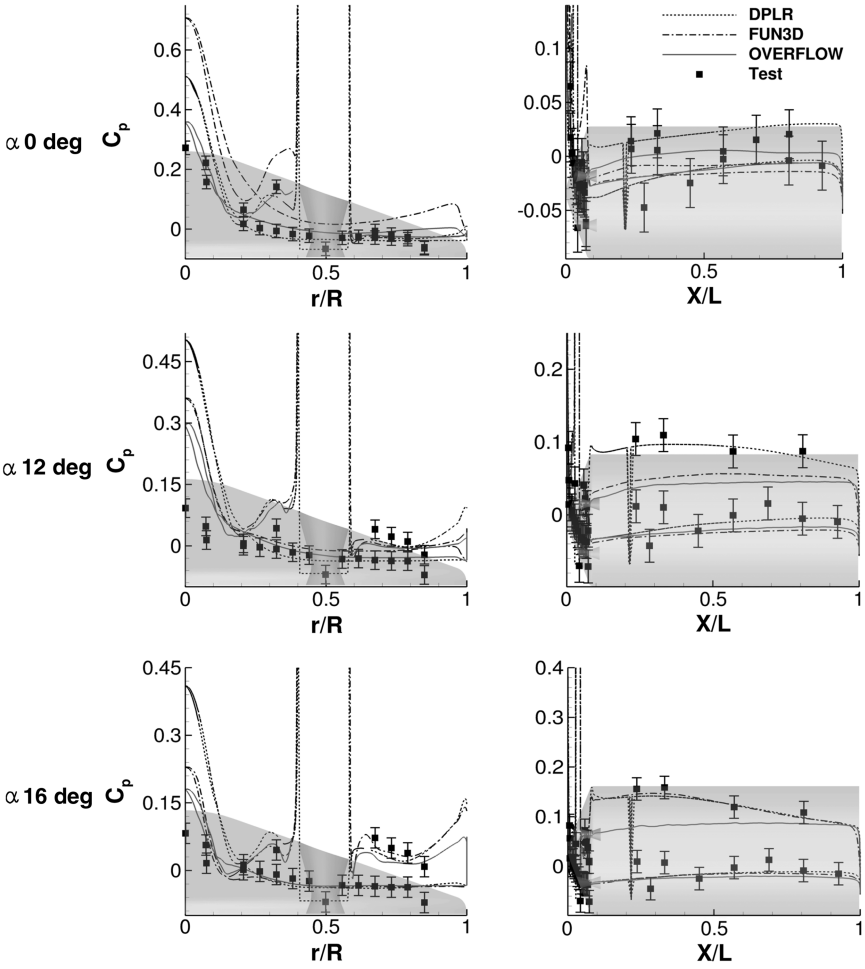

a) Comparison of time-averaged surface C_P

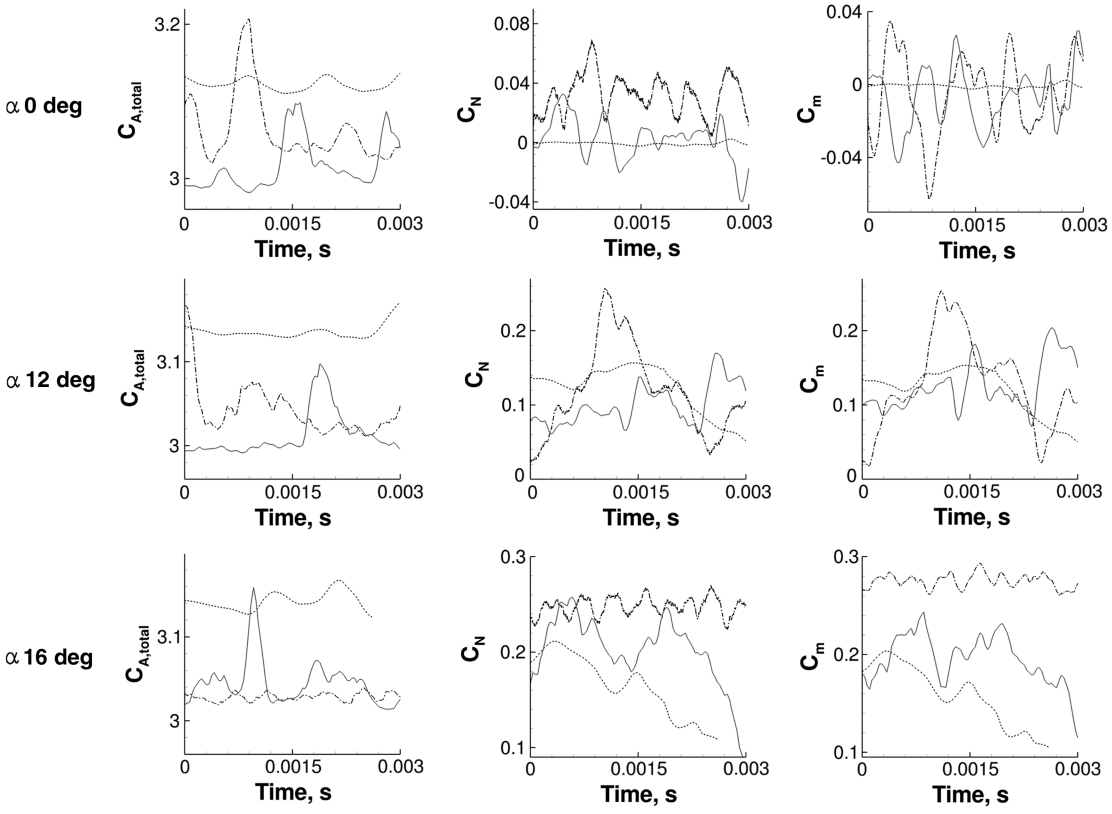

b) Code-to-code comparison of $C_{A,\text{total}}$, C_N, and C_m

Fig. 20 Comparisons of a) surface C_P, and b) $C_{A,\text{total}}$, C_N, and C_m as a function of time for run 263: three-nozzle, $C_T = 3$, $\phi = 180$ deg.

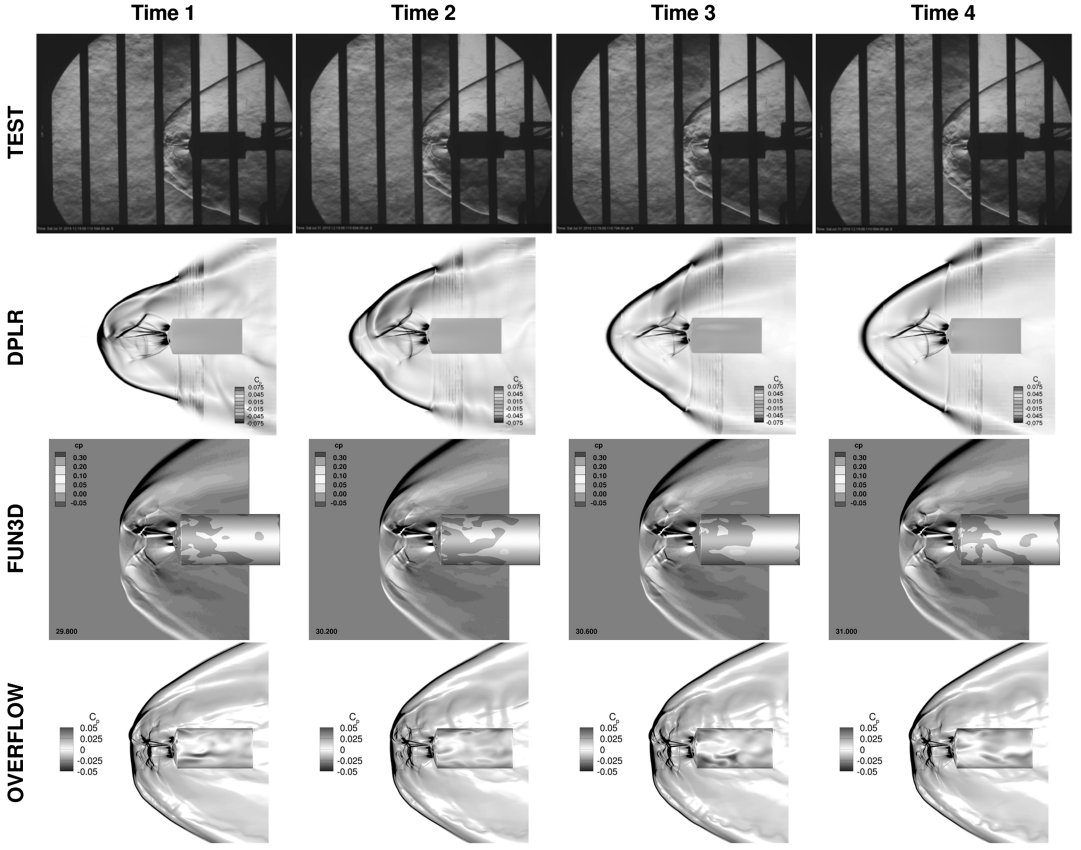

Fig. 21 Flow visualizations of run 307:, $\alpha = 0$ deg, $\phi = 0$ deg, four-nozzle, $C_T = 2$.

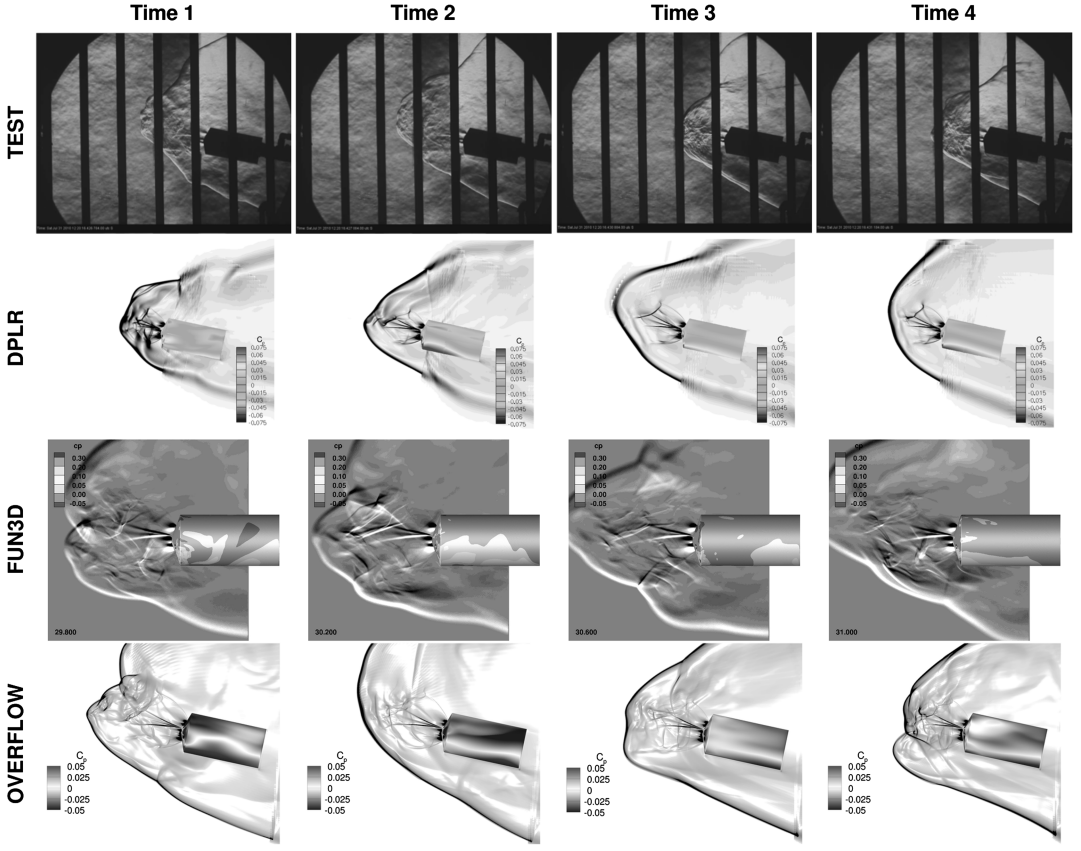

Fig. 22 Flow visualizations of run 307: $\alpha = 12$ deg, $\phi = 0$ deg, four-nozzle, $C_T = 2$.

part, all codes predict C_P well on the side of the model, except OVERFLOW underpredicts aft of the shoulder for $\alpha = 12$ deg, and FUN3D underpredicts aft of the shoulder for $\alpha = 20$ deg. On the model face, all three codes predict the leeward C_P well, but larger deviations are seen on the windward side. On the windward side, OVERFLOW underpredicts for $\alpha = 12$ deg, and all codes underpredict for $\alpha = 20$ deg.

F. Run 311: Four-Nozzle, $C_T = 2, \phi = 180\times$ *Degrees*

The same steadier behavior seen in run 307 at $\alpha = 0$ deg was seen in run 311 at $\alpha = 0$ deg, which was expected because the conditions are nearly the same. This behavior (Fig. 26) was properly simulated by DPLR and FUN3D (Fig. 29). OVERFLOW predicted an unsteady bow shock behavior that oscillated between nearly correct and very large standoff distances. Even with the differences in behavior, the C_P on the model face (Fig. 30) was similar to that seen for run 307 at $\alpha = 0$ deg. On the side of the model, OVERFLOW predicted lower pressure than DPLR and FUN3D but was mostly still inside the tunnel uncertainty.

For $\alpha = 12$ deg (Fig. 27), a steadier mode was observed experimentally where the windward bow shock was somewhat stable, and the leeward bow shock showed an unsteady oscillatory shedding. This behavior was predicted most accurately by DPLR. Toward the end of the test Schlieren video, this mode shifted to a behavior similar to that seen in the OVERFLOW results.

Figure 28 shows that an even steadier mode was observed in the $\alpha = 20$ deg than the $\alpha = 12$ deg case. FUN3D and OVERFLOW capture this mode, while the DPLR results were unsteady. All codes predict the average surface C_P well except for on the windward face between the peripheral nozzle and shoulder and just aft of the shoulder on the windward side.

VI. Discussion of Results

One of the largest differences in the code-to-code comparison was the level of unsteadiness predicted by each solver. DPLR used the vorticity-based production term, while OVERFLOW used the strain-based production term with the realizability constraint. OVERFLOW used DES with SST as the submodel for the one- and three-nozzle cases, and RANS SST for the zero- and four-nozzle cases. FUN3D used DES with SA as the submodel for blowing cases and vorticity based SST for the zero-nozzle cases. Each of these turbulence models generates different levels of eddy viscosity, which adds dissipation to the solutions, making them more steady [15]. Generally speaking, the

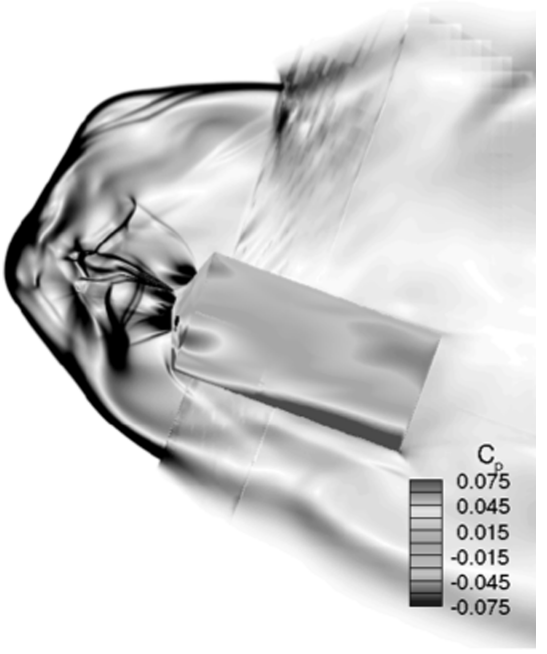

Fig. 24 Close-up DPLR flow visualizations of run 307: $\alpha = 20$ deg, $\phi = 0$ deg, four-nozzle, $C_T = 2$.

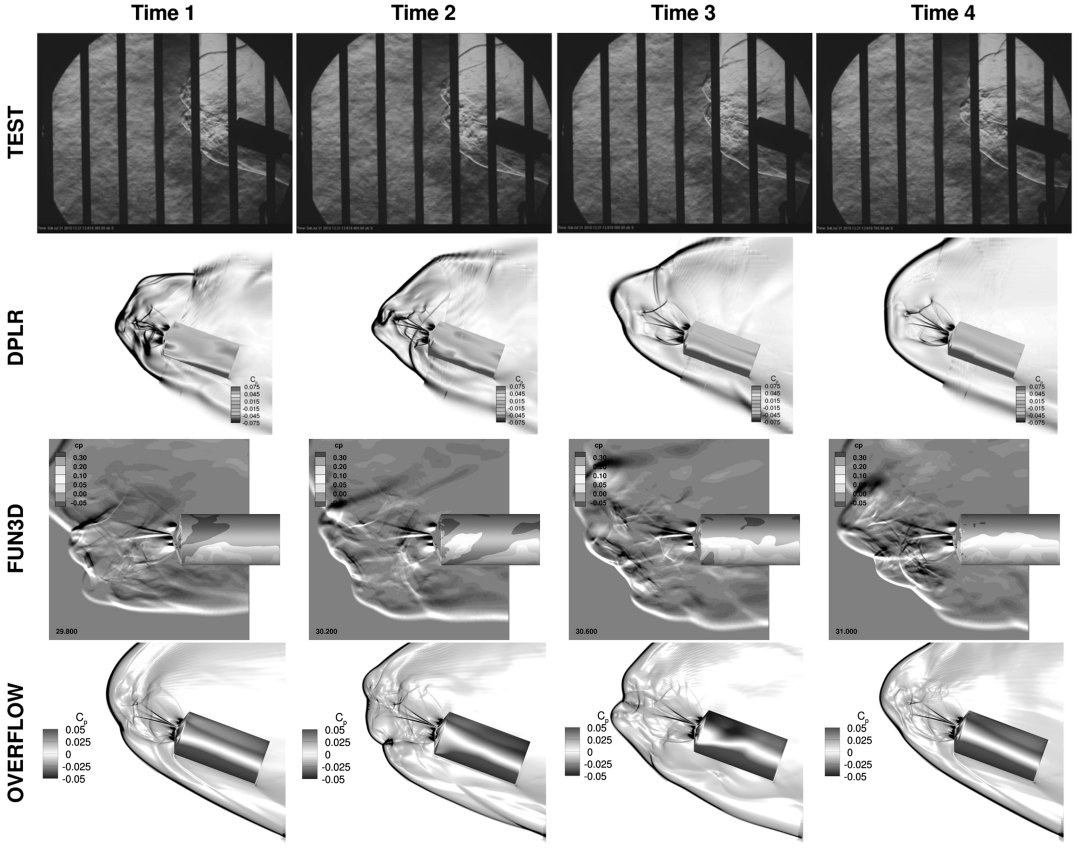

Fig. 23 Flow visualizations of run 307: $\alpha = 20$ deg, $\phi = 0$ deg, four-nozzle, $C_T = 2$.

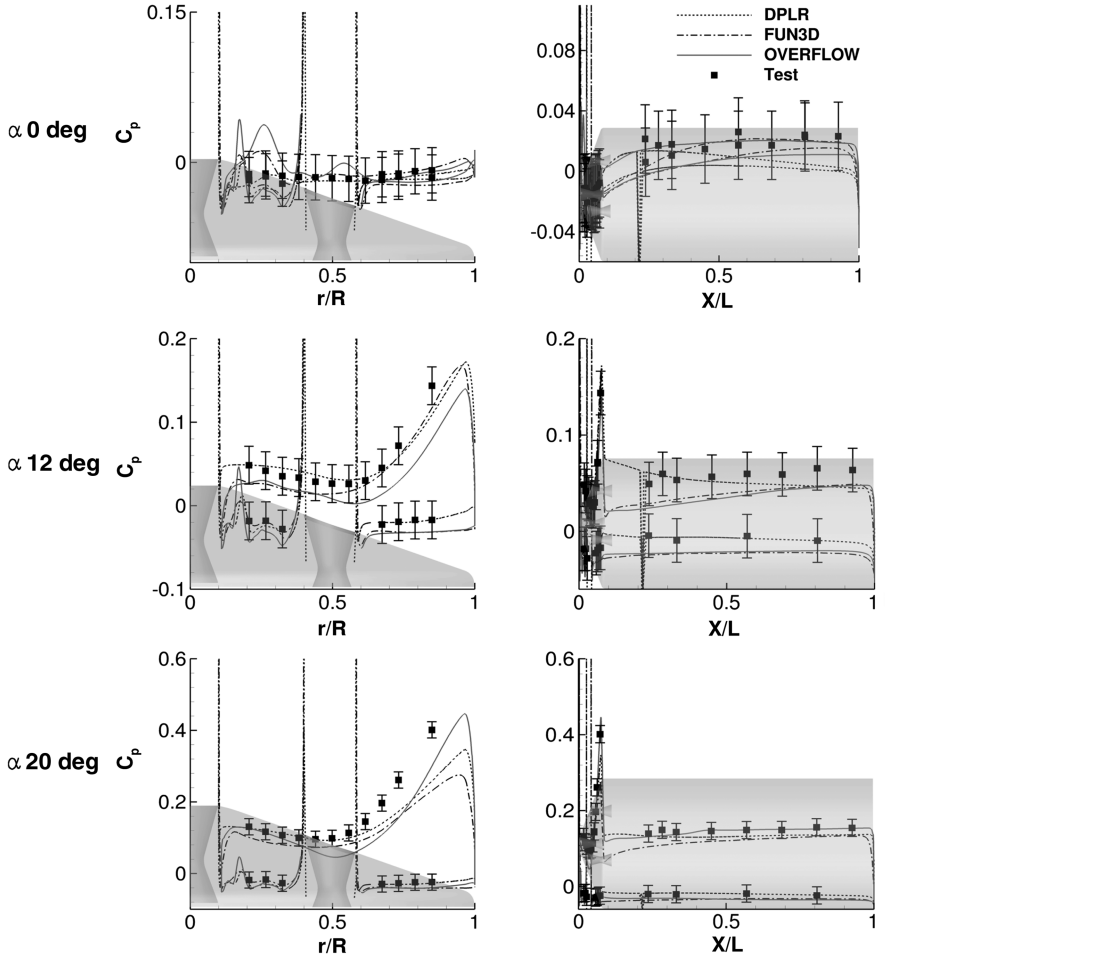

a) Comparison of time-averaged surface C_P

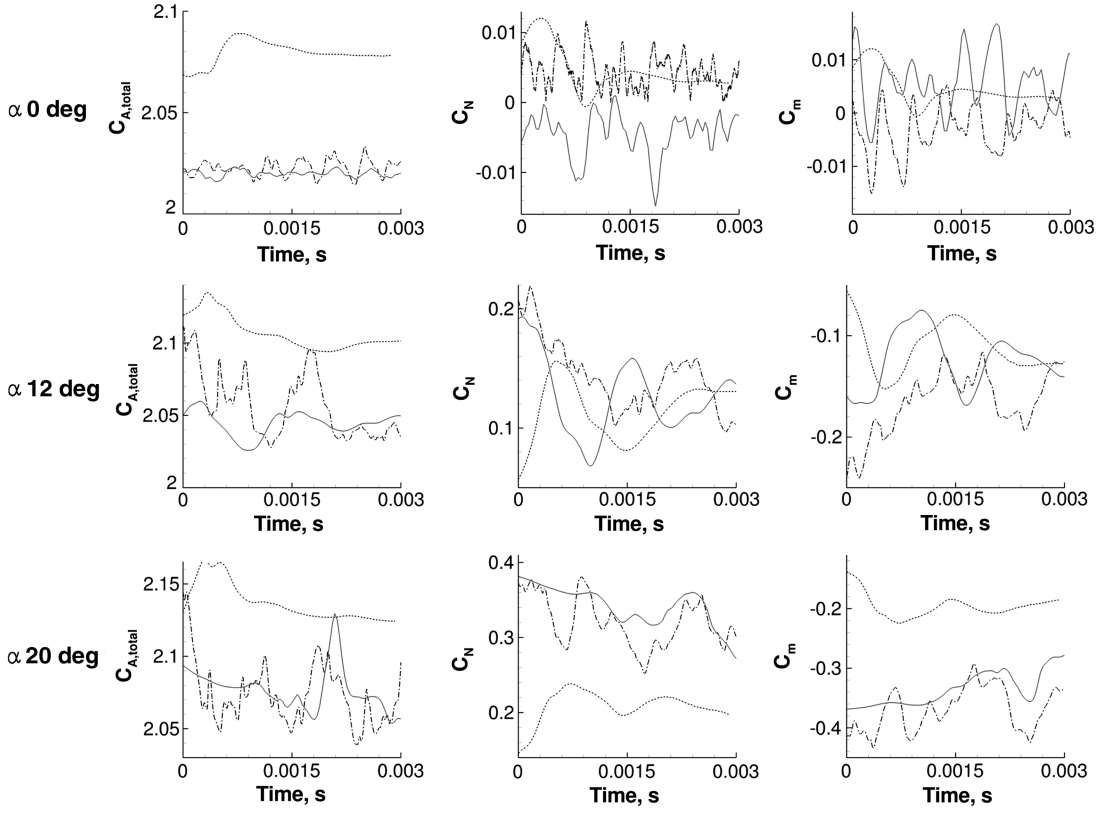

b) Code-to-code comparison of $C_{A,\text{total}}$, C_N, and C_m

Fig. 25 Comparisons of a) surface C_P, and b) $C_{A,\text{total}}$, C_N, and C_m as a function of time for run 307: four-nozzle, $C_T = 2, \phi = 0$ deg.

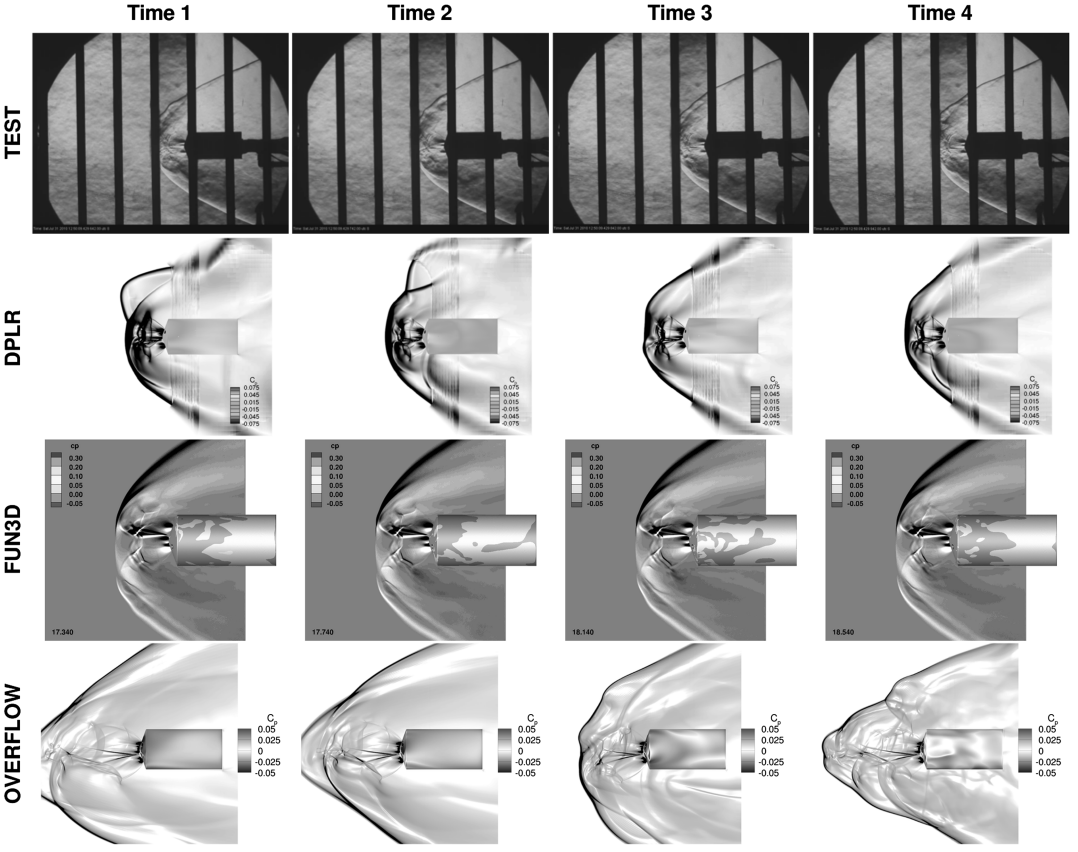

Fig. 26 Flow visualizations of run 311: $\alpha = 0$ deg, $\phi = 180$ deg, four-nozzle, $C_T = 2$.

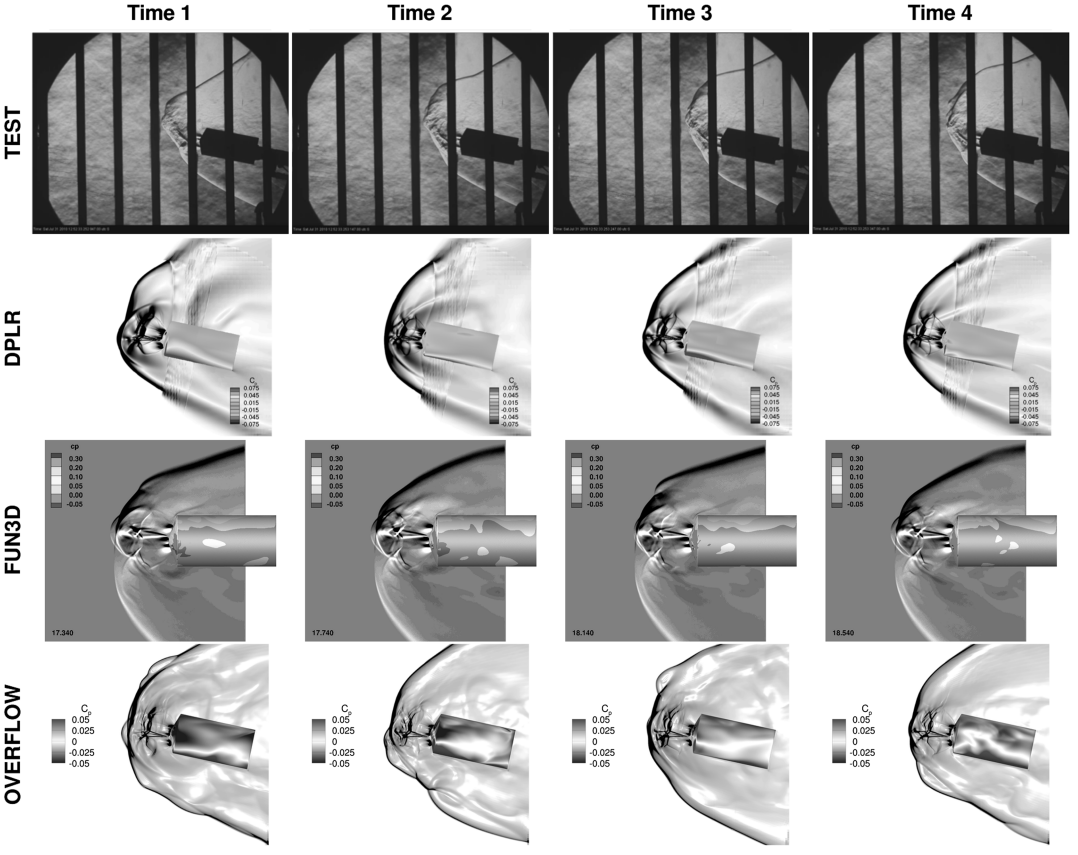

Fig. 27 Flow visualizations of run 311: $\alpha = 12$ deg, $\phi = 180$ deg, four-nozzle, $C_T = 2$.

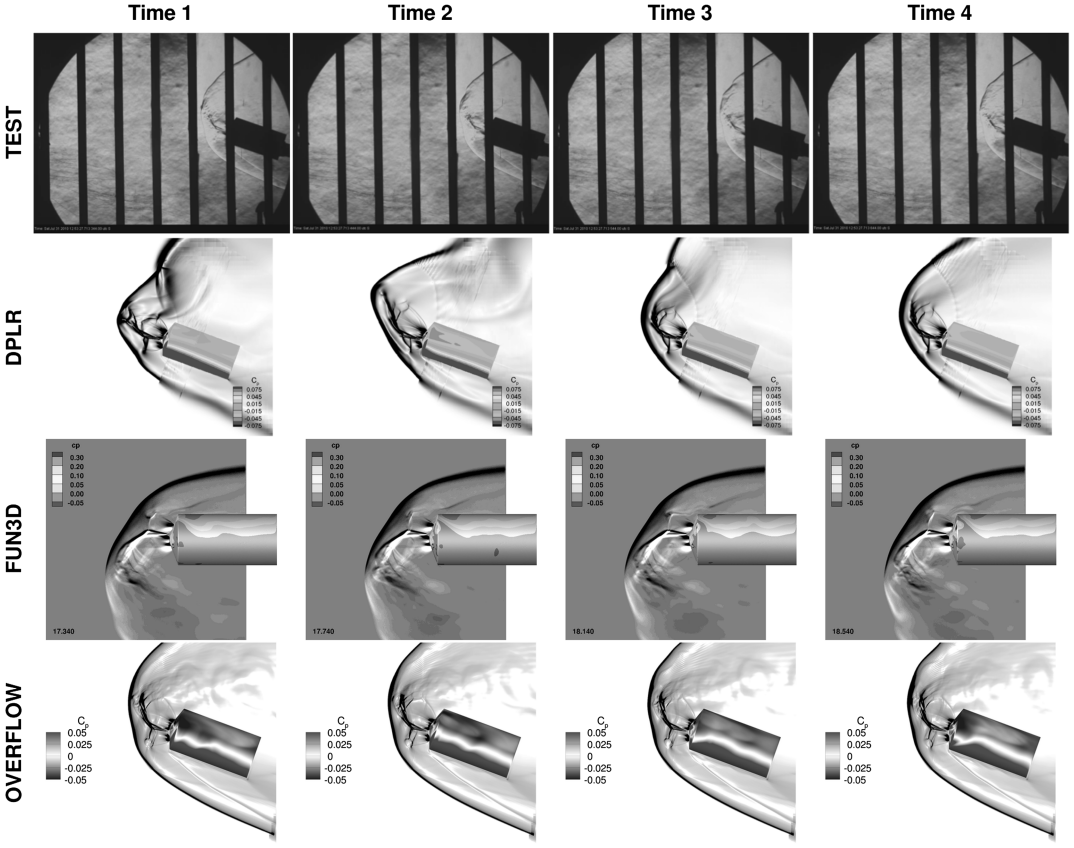

Fig. 28 Flow visualizations of run 311: $\alpha = 20$ deg, $\phi = 180$ deg, four-nozzle, $C_T = 2$.

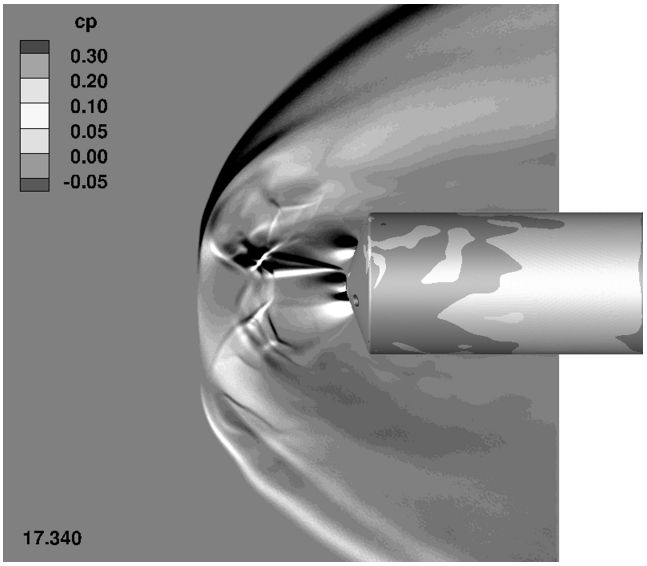

Fig. 29 Close-up FUN3D flow visualizations of run 311: $\alpha = 0$ deg, $\phi = 180$ deg, four-nozzle, $C_T = 2$.

RANS models were more steady than the DES, and the vorticity based SST models were more steady than the strain based with realizability constraint, although grid resolution and code implementation may also contribute significantly to those trends.

Another significant difference between the CFD predictions is the grid resolution used with each solver. Even though refinement for all grids is focused on the plume region, differences in spacing and topology do exist; see [15]. The level of unsteadiness is influenced by the level of dissipation, which can be increased by the coarseness of the grid.

The ability to properly capture the unsteady effects had varying effect on matching test-averaged surface C_P. Solving the simulations time-accurately took large computational resources to obtain an average. It was shown that, in some circumstances, a solution trending toward steady state compared as well as one that captured the unsteady effects (for example, run 262 $\alpha = 16$ deg or run 311 $\alpha = 20$ deg). For other cases, it seemed the unsteady effects were important (for example, run 165 $\alpha = 0$ deg). No specific trend was established, meaning a case-by-case inspection would be required. To be able to predict an SRP flowfield where test or flight data are not available, a time-accurate approach that captures the unsteady effects would be required because a steady-state solution may not be sufficient or exist.

Obtaining a proper time average for such an unsteady flowfield was an issue with the CFD results. A small time step was required to resolve the high-frequency unsteadiness, and yet a large amount of time is needed to define an average. The periodic unsteady behavior seen in run 165 at $\alpha = 0$ deg was more conducive to calculating a proper average, but for other cases, the unsteadiness was random, and no periodicity was noted. It was possible for the CFD simulations to resolve a certain section of the unsteady behavior and obtain a converged average but still not cover the entire 2.5 s of the test data-acquisition window. By this, the CFD and wind-tunnel data may have reached different averages.

For the wind tunnel, the pressure taps (exempting the high-frequency gauges) took 25 or 75 readings over 2.5 s, giving rates of 10 or 30 readings per second. For the CFD results, total simulation times were under 0.05 s with thousands of data points for averaging. The wind-tunnel sample interval (0.1 or 0.033 s) is on the order of or greater than the total CFD simulation times. This means that flowfield variations with time scales longer than 0.1 s would be included in the average of the wind-tunnel data but missed by the CFD simulations. Conversely, flowfield variations less than the tunnel sample interval were captured and averaged by the CFD but missed by the wind-tunnel data-acquisition system.

With the inherent unsteadiness of the flowfield, vehicle stability becomes a concern. It is important to realize that the measured unsteadiness in the surface tap readings have a small contribution to the total axial force. Figure 31 shows the contributions of aero-

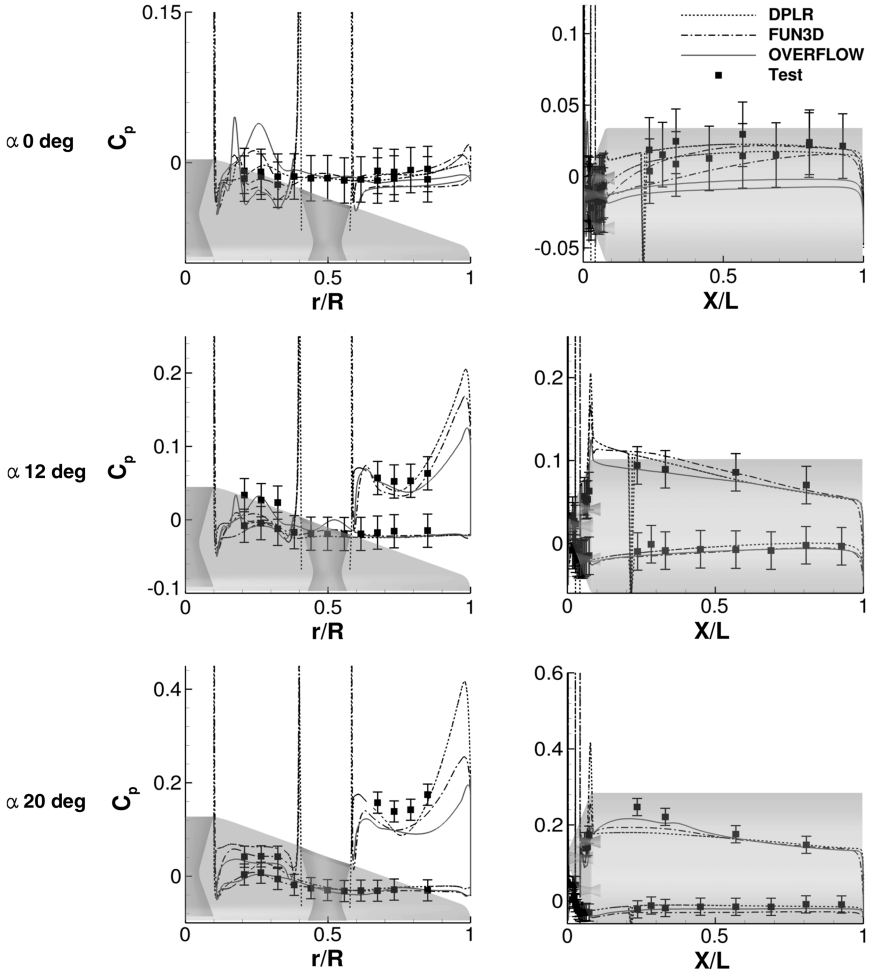

a) Comparison of time-averaged surface C_P

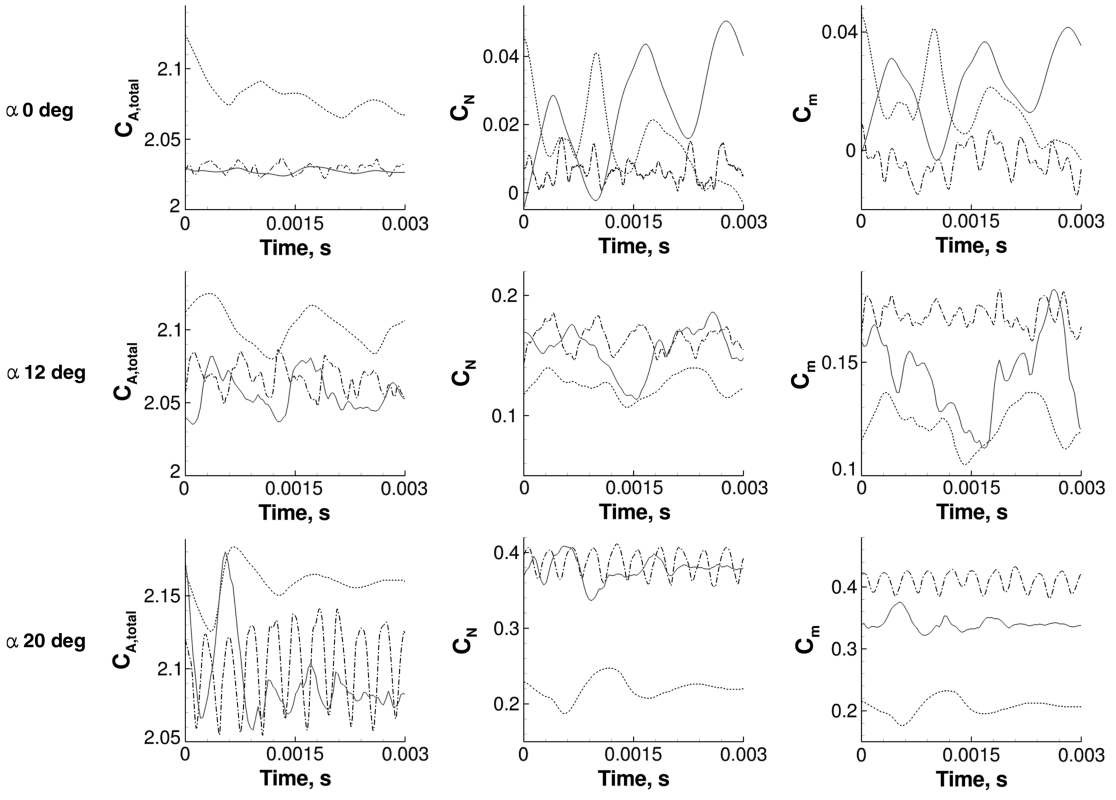

b) Code-to-code comparison of $C_{A,\text{total}}$, C_N, and C_m

Fig. 30 Comparisons of a) surface C_P, and b) $C_{A,\text{total}}$, C_N, and C_m as a function of time for run 311: four-nozzle, $C_T = 2, \phi = 180$ deg.

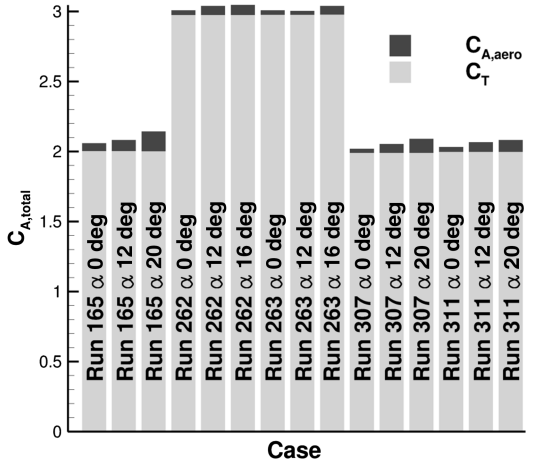

Fig. 31 Contributions of aerodynamic surface forces and thrust to the total axial force coefficient (OVERFLOW).

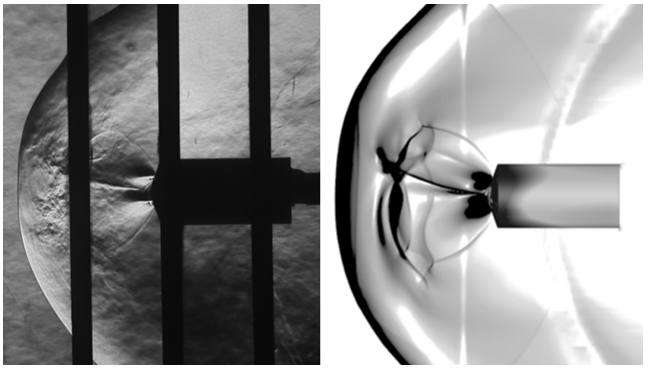

Fig. 32 Wind-tunnel Schlieren (left) and constructed Schlieren of OVERFLOW simulation (right) of the three-nozzle configuration at Mach 3.5 and $C_T = 6$.

dynamics and thrust to the overall axial force coefficient. In most cases, the surface aerodynamic forces contribute less than 5%. This should result in the surface pressures creating an even smaller percentage of the total axial force.

The required flight thrust coefficients will be much higher (∼10 s) than those achieved in the test. Thrust coefficients this large were not obtained in this test due to tunnel interference. A couple runs were made for the three-nozzle configuration at $\alpha = 0$ deg with C_T values as high as six. At this higher thrust coefficient, the flow was more steady as seen in Fig. 32, and the contribution of aerodynamic effects to the total axial force was much less than for smaller thrust coefficients. Future plans of the project is to take the same 5-in.-diameter model into the NASA Ames 9×7 ft Unitary Plan Wind Tunnel. With the larger test section, tunnel wall effects will be lessened, and higher thrust coefficients will be possible.

VII. Conclusions

Computational fluid dynamics has taken a strong step toward validation for supersonic retropropulsion. Using three solvers, Data Parallel Line Relaxation, Fully Unstructured Navier–Stokes Three-Dimensional, and OVERset grid FLOW solver, comparisons were made to test 1853 from the Langley Unitary Plan Wind Tunnel. Code-to-code and code-to-test comparisons are encouraging, and possible error sources have been defined. The level of unsteadiness predicted by each code varied and was largely dependent on grid resolution and turbulence model. A trend was seen that Reynolds-averaged Navier–Stokes models were more steady than detached-eddy simulation models, and vorticity-based shear-stress transport models are more steady than strain-based shear-stress transport models using the realizability constraint. Large differences in data-acquisition rates between the flow solvers and the wind-tunnel system may contribute to average surface pressure coefficient error. The level of contribution of the unsteady effects to the average surface pressure coefficient varied by case, making a time-accurate simulation necessary for predicting SRP flowfields. An inherent unsteadiness was noted at the tested thrust coefficients, but it was shown that the flowfield is much steadier at higher thrust coefficients for the three-nozzle configuration.

Acknowledgments

Pieter G. Buning of NASA Langley Research Center, Hampton, Virginia; Phillip C. Stuart and Darby J. Vicker of NASA Johnson Space Center, Houston, Texas; and Thomas M. Booth of Jacobs Technology, Houston, Texas, provided valuable guidance on gridding and solver best practices for OVERFLOW. William T. Jones of NASA Langley Research Center, Hampton, Virginia, provided the GridEx/batchEx unstructured grid generation framework and helped with its application to generate FUN3D grids. Todd R. White and Andrew J. Hyatt of ERC Inc., Moffett Field, California, helped develop DPLR best practices and provided overset gridding assistance for DPLR cases. David A. Saunders of ERC Inc., Moffett Field, California, developed the code used for OVERFLOW and DPLR simulated Schlieren/shadowgraph visualizations. The authors would like to acknowledge the support of the Exploration Technology Development and Demonstration (ETDD) Program, which was managed at NASA Glenn Research Center. The work documented herein was performed as part of ETDD's Entry, Descent, and Landing Technology Development Project, which was managed at NASA Langley Research Center and supported by NASA Ames Research Center, NASA Johnson Space Center, and the Jet Propulsion Laboratory.

References

[1] Braun, R. D., and Manning, R. M., "Mars Exploration Entry, Descent, and Landing Challenges," *Journal of Spacecraft and Rockets*, Vol. 44, No. 2, 2007, pp. 310–323. doi:10.2514/1.25116

[2] Steinfeldt, B. A., Theisinger, J. E., Korzun, A. M., Clark, I. G., Grant, M. J., and Braun, R. T., "High Mass Mars Entry, Descent, and Landing Architecture Assessment," *AIAA SPACE 2009 Conference and Exposition*, AIAA Paper 2009-6684, Sept. 2009.

[3] Zang, T. A., Dwyer–Dianciolo, A. M., Kinney, D. J., Howard, A. R., Chen, G. T., Ivanov, M. C., Sostaric, R. R., and Westhelle, C. H., "Overview of the NASA Entry, Descent and Landing Systems Analysis Study," *AIAA SPACE 2010 Conference and Exposition*, AIAA Paper 2010-8649, Aug. 2010.

[4] Edquist, K. T., Dyakonov, A. A., Korzun, A. M., Shidner, J. D., Studak, J. W., Tigges, M. A., Kipp, D. M., Prakash, R., Trumble, K. A., and Dupzyk, I. C., "Development of Supersonic Retro-Propulsion for Future Mars Entry, Descent, and Landing Systems" (to be published).

[5] Korzun, A. M., and Braun, R. D., "Performance Characterization of Supersonic Retropropulsion for High-Mass Mars Entry Systems," *Journal of Spacecraft and Rockets*, Vol. 47, No. 5, 2010, pp. 836–848. doi:10.2514/1.49803

[6] Korzun, A. M., Braun, R. D., and Cruz, J. R., "Survey of Supersonic Retropropulsion Technology for Mars Entry, Descent, and Landing," *Journal of Spacecraft and Rockets*, Vol. 46, No. 5, 2009, pp. 929–937. doi:10.2514/1.41161

[7] Trumble, K. A., Schauerhamer, D. G., Kleb, W. L., Carlson, J. R., Buning, P. G., Edquist, K. T., and Barnhardt, M. D., "An Initial Assessment of Navier–Stokes Codes Applied to Supersonic Retro-Propulsion," *10th AIAA/ASME Joint Thermophysics and Heat Transfer Conference*, AIAA Paper 2010-5047, June 2010.

[8] Trumble, K. A., Schauerhamer, D. G., Kleb, W. L., Carlson, J. R., and Edquist, K. T., "Analysis of Navier–Stokes Codes Applied to Supersonic Retro-Propulsion Wind Tunnel Test" (to be published).

[9] Wright, M. W., White, T., and Mangini, N., "Data Parallel Line Relaxation (DPLR) Code User Manual Acadia Version 4.01.1," NASA TM-2009-215388, Oct. 2009.

[10] Anderson, W. K., and Bonhaus, D. L., "An Implicit Upwind Algorithm for Computing Turbulent Flows on Unstructured Grids," *Computers and Fluids*, Vol. 23, No. 1, 1994, pp. 1–21. doi:10.1016/0045-7930(94)90023-X

[11] Anderson, W. K., Rausch, R. D., and Bonhaus, D. L., "Implicit/Multigrid Algorithm for Incompressible Turbulent Flows on

Unstructured Grids," *Journal of Computational Physics*, Vol. 128, No. 2, 1996, pp. 391–408.
doi:10.1006/jcph.1996.0219

[12] Buning, P. G., Jespersen, D. C., Pulliam, T. H., Klopfer, G. H., Chan, W. M., Slotnick, J. P., Krist, S. E., and Renze, K. J., "OVERFLOW User's Manual," NASA Langley Research Center, Hampton, VA, 2002.

[13] Berry, S. A., and Rhode, M. N., "Supersonic Retro-Propulsion Test 1853 in NASA LaRC Unitary Plan Wind Tunnel Test Section 2," NASA EDL-01-TR-9178, Nov. 2010.

[14] Berry, S. A., Laws, C. T., Kleb, W. L., Rhode, M. N., Spells, C., Mccrea, A. C., Trumble, K. A., Schauerhamer, D. G., and Oberkampf, W. L., "Design and Analysis of a Supersonic Retropropulsion Validation Experiment in the NASA Langley Unitary Plan Wind Tunnel Test" (to be pulished).

[15] Kleb, W. L., Schauerhamer, D. G., Trumble, K. A., Sozer, E., Barnhardt, M. D., Carlson, J. R., and Edquist, K. T., "Toward Supersonic Retropropulsion CFD Validation" (to be published).

[16] Jarvinen, P. O., and Adams, R. H., "The Aerodynamic Characteristics of Large Angled Cones with Retrorockets," NASA CR-NAS7-576, Feb. 1970.

[17] Bakhtian, N. M., and Aftosmis, M. J., "Parametric Study of Peripheral Nozzle Configurations for Supersonic Retropropulsion," *Journal of Spacecraft and Rockets*, Vol. 47, No. 6, 2010, pp. 935–950.
doi:10.2514/1.48887

[18] MacCormack, R. W., and Candler, G. V., "The Solution of the Navier–Stokes Equations Using Gauss–Seidel Line Relaxation," *Computers and Fluids*, Vol. 17, No. 1, 1989, pp. 135–150.
doi:10.1016/0045-7930(89)90012-1

[19] van Leer, B., "Towards the Ultimate Conservative Scheme. V. A Second–Order Sequel to Godunov's Method," *Journal of Computational Physics*, Vol. 32, No. 1, 1979, pp. 101–136.
doi:10.1016/0021-9991(79)90145-1

[20] Yee, H. C., "A Class of High-Resolution Explicit and Implicit Shock Capturing Methods," NASA TM-101088, Feb. 1989.

[21] Menter, F. R., "Two-Equation Eddy-Viscosity Turbulence Models for Engineering Applications," *AIAA Journal*, Vol. 32, No. 8, 1994, pp. 1598–1605.
doi:10.2514/3.12149

[22] Edwards, J. R., "A Low-Diffusion Flux-Splitting Scheme for Navier–Stokes Calculation," *Computers and Fluids*, Vol. 26, No. 6, 1997, pp. 653–659.
doi:10.1016/S0045-7930(97)00014-5

[23] van Albada, G. D., van Leer, B., and Roberts, W. W., "A Comparative Study of Computational Methods in Cosmic Gas Dynamics," *Astronomy and Astrophysics*, Vol. 108, No. 1, 1982, pp. 76–84.

[24] Vatsa, V. N., and White, J. A., "Calibration of a Unified Flux Limiter for Ares-Class Launch Vehicles from Subsonic to Supersonic Speeds," *56th Propulsion Meeting 5*, JANNAF Paper III, April 2009.

[25] White, J. A., private communication, 2010.

[26] Spalart, P. R., and Allmaras, S. R., "A One-Equation Turbulence Model for Aerodynamic Flows," *30th Aerospace Sciences Meeting and Exhibit*, AIAA Paper 1992-0439, Jan. 1992.

[27] Vatsa, V. N., Carpenter, M. H., and Lockard, D. P., "Re-Evaluation of an Optimized Second Order Backward Difference (BDF2OPT) Scheme for Unsteady Flow Applications," *48th AIAA Aerospace Sciences Meeting*, AIAA Paper 2010-0122, Jan. 2010.

[28] Tramel, R., Nichols, R., and Buning, P., "Addition of Improved Shock-Capturing Schemes to OVERFLOW 2.1," *19th AIAA Computational Fluid Dynamics*, AIAA Paper 2009-3988, June 2009.

[29] Wilcox, D. C., "Formulation of the κ-ω Turbulence Model Revisited," *AIAA Journal*, Vol. 46, No. 11, 2008, pp. 2823–2838.
doi:10.2514/1.36541

[30] Rhode, M. N., and Oberkampf, W. L., "Estimation of Uncertainties for Supersonic Retropropulsion Model Validation Experiment in a Wind Tunnel" (to be published).

[31] Aeschliman, D. P., and Oberkampf, W. L., "Experimental Methodology for Computational Fluid Dynamics Code Validation," *AIAA Journal*, Vol. 36, No. 5, 1998, pp. 733–741.
doi:10.2514/2.461

[32] Yates, L. A., "Interferograms, Schlieren, and Shadowgraphs Constructed from Real- and Ideal-Gas, Two- and Three-Dimensional Computed Flowfields," NASA CR-190054, Jan. 1992.

C. Chang
Associate Editor